Inorg. Chem. **2007**, *46*, 2373–2387

Synthesis, Structural Characterization, and Multifrequency Electron Paramagnetic Resonance Studies of Mononuclear Thiomolybdenyl Complexes

Simon C. Drew,[†,‡] Jason P. Hill,[§] Ian Lane,[†,‡] Graeme R. Hanson,*[,†,‡] Robert W. Gable,[§] and Charles G. Young*[,§]

Centre for Magnetic Resonance and Centre for Metals in Biology, University of Queensland, Queensland 4072, Australia, and School of Chemistry, University of Melbourne, Victoria 3010, Australia

Received April 6, 2006

Reaction of $Tp^*Mo^VSCl_2$ with a variety of phenols and thiols in the presence of triethylamine produces mononuclear, thiomolybdenyl complexes $Tp^*Mo^VSX_2$ [Tp* = hydrotris(3,5-dimethylpyrazol-1-yl)borate; X = 2-(ethylthio)phenolate (etp), 2-(n-propyl)phenolate (pp), phenolate; X_2 = benzene-1,2-dithiolate (bdt), 4-methylbenzene-1,2-dithiolate (tdt), benzene-1,2-diolate (cat)]. The complexes have been characterized by microanalysis, mass spectrometry, IR, EPR, and UV–visible spectroscopic data, and X-ray crystallography (for the etp, pp, bdt, and cat derivatives). The mononuclear, six-coordinate, distorted-octahedral Mo centers are coordinated by terminal sulfido (Mo≡S = 2.123(1)–2.1368(8) Å), tridentate *facial* Tp*, and monodentate or bidentate O/S–donor ligands. Multifrequency (S-, X-, Q-band) EPR spectra of the complexes and selected molybdenyl analogues were acquired at 130 K and 295 K and yielded a spin Hamiltonian of C_s symmetry or lower, with $g_{zz} < g_{yy} < g_{xx} < g_e$ and $A_{z'z'} > A_{x'x'} \approx A_{y'y'}$, and a noncoincidence angle in the range of $\beta = 24–39°$. Multifrequency EPR, especially at S-band, was found to be particularly valuable in the unambiguous assignment of the spin Hamiltonian parameters in these low-symmetry complexes. The weaker π-donor terminal sulfido ligand yields a smaller SOMO–LUMO gap and reduced *g*-values for the thiomolybdenyl complexes compared with molybdenyl analogues, supporting existing crystallographic and EPR data for an apically coordinated oxo group in the active site of xanthine oxidase.

Introduction

Molybdopterin (MPT)-Mo enzymes play vital roles in plant, animal, and human health, the carbon, sulfur, and nitrogen cycles, biofeedback systems, and the control of global climate.[1−5] The enzymes fall into three families based on sequence and structural similarities; these being the xanthine oxidase (Mo hydroxylases), sulfite oxidase, and dimethyl sulfoxide reductase families, named after their archetypical member. With the exception of CO dehydrogenase, the enzymes contain a mononuclear Mo active site coordinated by one or two bidentate MPT ligands and a complement of oxo, sulfido, water-based, and/or amino-acid ligands; the coordination number of Mo is typically five or six.[1−5] The enzymes cycle through the molybdenum oxidation states +6, +5, and +4 where Mo(V) (d^1) is paramagnetic. For the xanthine oxidase family of enzymes, the Mo(V) species are formed in the oxidative (Mo(IV) → Mo(VI)) portion of the reaction cycle which regenerates the resting enzyme. Electron paramagnetic resonance (EPR) signals are elicited from the active forms of the enzymes as well as inactive, inhibited, or other forms. The interrogation of paramagnetic states by electron magnetic resonance techniques such as EPR, electron nuclear double resonance

* To whom correspondence should be addressed. E-mail: cgyoung@unimelb.edu.au (C.G.Y.), graeme.hanson@cmr.uq.edu.au (G.R.H.).
† Centre for Magnetic Resonance, University of Queensland.
‡ Centre for Metals in Biology, University of Queensland.
§ University of Melbourne.

(1) Hille, R. *Chem. Rev.* **1996**, *96*, 2757.
(2) Pilato, R. S.; Stiefel, E. I. In *Bioinorganic Catalysis*, 2nd ed.; Reedijk, J., Bouwman, E., Eds.; Marcel Dekker: New York, 1999; pp 81−152.
(3) *Metal Ions in Biological Systems*; Sigel, A., Sigel, H., Eds.; Marcel Dekker: New York, 2002; Vol. 39.
(4) Tunney, J. M.; McMaster, J.; Garner, C. D. In *Comprehensive Coordination Chemistry II*; McCleverty, J. A., Meyer, T. J., Eds.; Elsevier Pergamon: Amsterdam, 2004; Vol. 8, Chapter 8.18, pp 459−477.
(5) Young, C. G. In *Encyclopedia of Inorganic Chemistry 2;* King, R. B., Ed.; Wiley: Chichester, U.K., 2005; Vol. V, pp 3321−3340.

10.1021/ic060585j CCC: $37.00
Published on Web 03/08/2007

(ENDOR), and electron spin echo envelope modulation (ESEEM) has provided a wealth of structural and mechanistic information.[6−10]

The Mo hydroxylases, e.g., xanthine oxidase/dehydrogenase and aldehyde oxidoreductase, catalyze substrate hydroxylation or transhydroxylation reactions and feature oxosulfido-Mo(VI) active sites bearing hydroxo and MPT coligands.[1−5] The sulfido group is mandatory for catalysis, its removal by cyanide producing inactive desulfo forms of the enzymes. The active site of xanthine oxidase is now relatively well understood. It contains a square pyramidal (or pseudotetrahedral) $[(MPT)MoOS(OH)]^-$ moiety, possessing an apical oxo ligand and basal dithiolene, sulfido, and hydroxo ligands. Earlier crystallographic evidence for an apical sulfido group[11] is not supported by the most recent diffraction data.[12] The presence of a hydroxo ligand (rather than aqua) in the active enzyme is supported by recent extended X-ray absorption fine structure (EXAFS) studies by Doonan et al.[13] Oxosulfido-Mo(V) centers are implicated in the turnover of the enzymes under substrate limiting conditions, the very rapid EPR signal being ascribed to a center of this type.[14] EPR and related studies of oxosulfido anions such as $[(L\text{-}N_2S_2)MoOS]^-$ (particularly ^{95}Mo, ^{98}Mo, ^{33}S, and ^{17}O labeled species; L-N_2S_2 = *N*,*N*′-dimethyl-*N*,*N*′-bis(2-mercaptophenyl)-1,2-diaminoethane) and $[Tp^xMoOSX]^-$ (Tp^x = hydrotrispyrazolylborate derivative)[15] support this assignment. However, the EPR spectra of known oxosulfido-Mo(V) complexes have lower $\langle g \rangle$ values (<1.954) and are more anisotropic ($\Delta g > 0.124$) than the very rapid EPR signals ($\langle g \rangle = 1.9765$ and $\Delta g = 0.0758$ for xanthine oxidase). This behavior may reflect the presence of (i) a pterin dithiolene ligand in the enzymes (absent to date from models), (ii) a five-coordinate metal center in the enzyme (again, absent from models), and/or (iii) ligand-protein interactions or rearrangement of the $[Mo^VOS]^+$ center during catalysis. Detailed spectroscopic and theoretical studies of mononuclear oxosulfido-Mo(V) and sulfido-Mo(V) (thiomolybdenyl) complexes are essential in defining the nature of sulfido-Mo entities and for understanding the nature and properties of the very rapid and related EPR signals from Mo hydroxylases.

Molybdenyl ($[Mo^V{\equiv}O]^{3+}$) complexes have been known for many decades, and their chemical, structural, spectroscopic, and electronic properties are well documented.[16,17] EPR spectroscopy is routinely employed in the characterization of these species, the isotropic spectra displaying a strong central resonance (for $I = 0$ nuclei, 75%) and six flanking hyperfine satellites (due to ^{95,97}Mo, $I = 5/2$, 25%) characteristic of molybdenum. Particular classes of complexes have been extensively studied by EPR techniques. Chief among these are the molybdenyl halides, e.g., $[MoOX_5]^{2-}$ and $[MoOX_4(OH_2)]^-$ (X = halide), thiolates $[MoO(SR)_4]^-$, and hydrotris(3,5-dimethylpyrazol-1-yl)borate (Tp*) complexes, Tp*$MoOX_2$ (X/X_2 = mono- and bidentate N-, O-, and S-donors).

The simple, high-symmetry molybdenyl halides have attracted much attention, and earlier bonding descriptions[18] have been refined by ENDOR,[19] single-crystal EPR,[20,21] MCD,[22,23] and computational studies. The electronic structural contributions to the *g*-values of these complexes have been examined by Westmoreland and co-workers using a linear combination of atomic orbitals (LCAO) model.[20,21]

Complexes of the type, $[MoO(SR)_4]^-$, feature biologically relevant thiolate ligands.[17] The seminal work of Wedd and

(6) General reviews include the following: Bray, R. C. In *Biological Magnetic Resonance*; Reuben, J., Berliner, L. J., Eds.; Plenum Press: New York, 1980; pp 45−84. Cramer, S. P. *Adv. Inorg. Bioinorg. Mech.* **1983**, *2*, 259. Bray, R. C. *Q. Rev. Biophys.* **1988**, *21*, 299.

(7) For xanthine oxidases: George, G. N.; Bray, R. C. *Biochemistry* **1988**, *27*, 3603. Wilson, G. L.; Greenwood, R. J.; Pilbrow, J. R.; Spence, J. T.; Wedd, A. G. *J. Am. Chem. Soc.* **1991**, *113*, 6803. Greenwood, R. J.; Wilson, G. L.; Pilbrow, J. R.; Wedd, A. G. *J. Am. Chem. Soc.* **1993**, *115*, 5385. Lowe, D. J. In *Metal Ion in Biological Systems*; Sigel, A., Sigel, H., Eds.; Vol. 39, pp 455−480.

(8) For sulfite oxidases and sulfite dehydrogenase: Raitsimring, A. M.; Pacheco, A.; Enemark, J. H. *J. Am. Chem. Soc.* **1998**, *120*, 11263. Astashkin, A. V.; Mader, M. L.; Enemark, J. H.; Pacheco, A.; Raitsimring, A. M. *J. Am. Chem. Soc.* **2000**, *122*, 5294. Astashkin, A. V.; Raitsimring, A. M.; Fenf, C.; Johnson, J. L.; Rajagopalan, K. V.; Enemark, J. H. *J. Am. Chem. Soc.* **2002**, *124*, 6109. Astashkin, A. V.; Fenf, C.; Raitsimring, A. M.; Enemark, J. H. *J. Am. Chem. Soc.* **2005**, *127*, 500. Hemann, C.; Hood, R. L.; Fulton, M.; Aänsch, R.; Schwarz, G.; Mendel, R. R.; Kirk, M. L.; Hille, R. *J. Am. Chem. Soc.* **2005**, *127*, 16567. Raitsimring, A. M.; Kappler, U.; Feng, C.; Astashkin, A. V.; Enemark, J. H. *Inorg. Chem.* **2005**, *44*, 7283.

(9) For DMSO reductase: Bennett, B.; Benson, N.; McEwan, A. G.; Bray, R. C. *Eur. J. Biochem.* **1994**, *225*, 321. George, G. N.; Hilton, J.; Temple, C.; Prince, R. C.; Rajagopalan, K. V. *J. Am. Chem. Soc.*, **1999**, *121*, 1256. Raitsmiring, A. M.; Astashkin, A. V.; Feng, C. J.; Enemark, J. H.; Nelson, K. J.; Rajagopalan, K. V. *J. Biol. Inorg. Chem.* **2003**, *8*, 95. Enemark, J. H.; Astashkin, A. V.; Raitsmiring, A. M. *Paramagnetic Reson. Metallobiomolecules ACS Symp. Ser.* **2003**, *858*, 179.

(10) For nitrate reductases: Butler, C. S.; Charnock, J. M.; Bennett, B.; Sears, H. J.; Reilly, A. J.; Ferguson, S. J.; Garner, C. D.; Lowe, D. J.; Thomson, A. J.; Berks, B. C.; Richardson, D. J. *Biochemistry* **1999**, *38*, 9000. Bennett, B.; Charnock, J. M.; Sears, H. J.; Berks, B. C.; Thomson, A. J.; Ferguson, S. J.; Garner, C. D.; Richardson, D. J. *Biochem. J.* **1996**, *317*, 557. Sears, H. J.; Bennett, B.; Spiro, S.; Thomson, A. J.; Richardson, D. J. *Biochem. J.* **1995**, *310*, 311. Bennett, B.; Berks, B. C.; Ferguson, S. J.; Thomson, A. J.; Richardson, D. J. *Eur. J. Biochem.* **1994**, *226*, 789. George, G. N.; Turner, N. A.; Bray, R. C.; Morpeth, F. F.; Boxer, D. H.; Cramer, S. P. *Biochem. J.* **1989**, *259*, 693.

(11) Dobbek, H.; Huber, R. In *Metal Ions In Biological Systems*; Sigel, A., Sigel, H., Eds.; Marcel-Dekker: New York, 2002; Vol. 39, pp 227−263.

(12) Okamoto, K.; Matsumoto, K.; Hille, R.; Eger, B. T.; Pai, E. F.; Nishino, T. *Proc. Natl. Acad. Sci. U.S.A.* **2004**, *101*, 7931.

(13) Doonan, C. J.; Stockert, A.; Hille, R.; George, G. N. *J. Am. Chem. Soc.* **2005**, *127*, 4518.

(14) Wilson, G. L.; Greenwood, R. J.; Pilbrow, J. R.; Spence, J. T.; Wedd, A. G. *J. Am. Chem. Soc.* **1991**, *113*, 6803.

(15) Xiao, Z.; Bruck, M. A.; Doyle, C.; Enemark, J. H.; Grittini, C.; Gable, R. W.; Wedd, A. G.; Young, C. G. *Inorg. Chem.* **1995**, *34*, 5950. Laughlin, L. J. Young, C. G. *Inorg. Chem.* **1996**, *35*, 1050. Smith, P. D.; Slizys, D. A.; George, G. N.; Young, C. G. *J. Am. Chem. Soc.* **2000**, *122*, 2946.

(16) Garner, C. D.; Charnock, J. M. In *Comprehensive Coordination Chemistry*; Wilkinson, G., Gillard, R. D., McCleverty, J. A., Eds.; Pergamon: Oxford, 1987; Vol. 3, Chapter 36.4, pp 1329−1374.

(17) Young, C. G. In *Comprehensive Coordination Chemistry II*; McCleverty, J. A., Meyer, T. J., Eds.; Elsevier Pergamon: Amsterdam, 2004; Vol. 4, Chapter 4.7, pp 415−527.

(18) Gray, H. B.; Hare, C. R. *Inorg. Chem.* **1962**, *1*, 363. Hare, C. R.; Bernal, I.; Gray, H. B. *Inorg. Chem.* **1962**, *1*, 831.

(19) Attanasio, D.; Funicello, M.; Suber, L. *Chem. Phys. Lett.* **1988**, *147*, 273.

(20) Balagopalakrishna, C.; Kimbrough, J. T.; Westmoreland, T. D. *Inorg. Chem.* **1996**, *35*, 7758.

(21) Swann, J.; Westmoreland, T. D. *Inorg. Chem.* **1997**, *36*, 5348.

(22) Sabel, D. M.; Gewirth, A. A. *Inorg. Chem.* **1994**, *33*, 148.

co-workers[24,25] has been followed by MCD and computational studies[26−28] and, most recently, ^{17}O ESEEM studies defining the hyperfine and quadrupole parameters of the oxo ligand in $[MoO(SPh)_4]^-$.[29]

The oxo analogues of the title complexes, viz., Tp*$MoOX_2$ (X/X_2 = range of mono- and bidentate O- and S-donors), are another extensively studied series of complexes and much has been learned about their electronic structure.[17] The EPR parameters for a vast array of derivatives have been documented in many papers.[17] A range of spectroscopic probes, including MCD spectroscopy, have been employed to study the electronic structure of arene-1,2-dithiolate complexes featuring the pseudodithiolene moiety.[23,30,31] These have revealed a highly covalent, pseudo-σ interaction between the redox active Mo d_{xy} orbital and the dithiolate in-plane combination of S p orbitals. The weak, low-energy transitions at $\sim$10 000 cm^{-1} in the optical spectra of these complexes were assigned to transitions from filled out-of-plane sulfur pπ orbitals to the in-plane metal d_{xy} orbital. Intense bands at $\sim$19 000 cm^{-1} were assigned to charge-transfer transitions involving the pseudo-σ orbitals. Very recently, complexes containing true dithiolene ligands were reported by Sproules et al.[32] The correlation of EPR parameters with electronic structure has been a focus of single-crystal EPR studies by Collison et al.[33] and Nipales and Westmoreland.[34] EPR and MCD studies of molybdenyl complexes containing heteroscorpionate ligands have also been reported.[35]

Along with studies of anionic dichalcogenido species containing L-N_2S_2, there have also been studies of molybdenyl complexes containing this ligand, viz. (L-N_2S_2)-MoOX.[36,37] These have included MCD and computational[38] studies and the determination of the principal components of **g** and their orientation for *cis,trans*-(L-N_2S_2)MoOX (X = Cl, SCH_2Ph) by single-crystal EPR spectroscopy.[39] The effects of geometry and electronic structure on EPR parameters for tetradentate N_2S_2 and N_2O_2 Mo(V) complexes have also been examined by computational methods.[40]

Other EPR-active Mo(V) systems were recently reviewed.[17] In summary, sustained investigations, spanning many decades and employing increasingly sophisticated EPR techniques, have provided profound insights into the spectroscopic properties and electronic structures of molybdenyl complexes.

In stark contrast, there is very little known about the spectroscopic properties and electronic structures of thiomolybdenyl ($[Mo^V{\equiv}S]^{3+}$) complexes. Unlike related molybdenyl complexes, these are difficult to prepare, and their general susceptibility to hydrolysis, redox, and polynucleation reactions has prevented systematic studies. The first thiomolybdenyl complex, Tp*$MoSCl_2$, was prepared by Young et al. in 1987, by reacting Tp*$MoOCl_2$ with boron sulfide;[41] it has been characterized by a wide range of techniques, including IR, electronic, EPR,[41] resonance Raman,[42] and X-ray absorption spectroscopy (XAS).[43] Subsequently, Young et al.[44] reported the synthesis and S K-edge XAS and X-band EPR studies of several derivatives of Tp*$MoSCl_2$ and the crystal structures of Tp*$MoS(etp)_2$ and Tp*MoS(bdt). Preliminary frozen solution EPR studies at X-band frequencies revealed that, contrary to expectations, the thiomolybdenyl complexes exhibited lower *g*-values than their molybdenyl analogues.[41,44] Sulfur K-edge XAS studies revealed a characteristic pre-edge feature associated with the terminal sulfido ligand.[43] Related complexes, e.g., $[Tp'MoS(S_2PR_2)]^+$ (Tp′= hydrobis(3-isopropylpyrazolyl)(5-isopropylpyrazolyl)borate) have been generated in solution and characterized by EPR spectroscopy.[45] A second type of mononuclear thiomolybdenyl complex is represented by $MoS(NRAr)_3$. This complex is a member of the series $MoE(NRAr)_3$ (E = O, S, Se, Te) and is prepared by the oxidation of $Mo(NRAr)_3$ by sulfur or ethylene sulfide. The $MoE(NRAr)_3$ complexes exhibit low-symmetry EPR spectra with $\mathbf{A}(^{95,97}Mo)$ values decreasing in the order Mo≡O > Mo≡S > Mo≡Se > Mo≡Te, consistent with increasing covalency and electronic delocalization with the heavier chalcogenides. The sulfido

(23) Carducci, M. D.; Brown, C.; Solomon, E. I.; Enemark, J. H. *J. Am. Chem. Soc.* **1994**, *116*, 11856.
(24) Hanson, G. R.; Brunette, A. A.; McDonell, A. C.; Murray, K. S.; Wedd, A. G. *J. Am. Chem. Soc.* **1981**, *103*, 1953.
(25) Hanson, G. R.; Wilson, G. L.; Bailey, T. D.; Pilbrow, J. R.; Wedd, A. G. *J. Am. Chem. Soc.* **1987**, *109*, 2609.
(26) McNaughton, R. L.; Tipton, A. A.; Rubie, N. D.; Conry, R. R.; Kirk, M. L. *Inorg. Chem.* **2000**, *39*, 5697.
(27) McMaster, J.; Carducci, M. D.; Yang, Y.-S.; Solomon, E. I.; Enemark, J. H. *Inorg. Chem.* **2001**, *40*, 687.
(28) McNaughton, R. L.; Mondal, S.; Nemykin, V. N.; Basu, P.; Kirk, M. L. *Inorg. Chem.* **2005**, *44*, 8216.
(29) Astashkin, A. V.; Neese, F.; Raitsimring, A. M.; Cooney, J. J. A.; Bultman, E.; Enemark, J. H. *J. Am. Chem. Soc.* **2005**, *127*, 16713.
(30) Helton, M. E.; Gruhn, N. E.; McNaughton, R. L.; Kirk, M. L. *Inorg. Chem.* **2000**, *39*, 2273.
(31) Inscore, F. E.; McNaughton, R.; Westcott, B. L.; Helton, M. E.; Jones, R.; Dhawan, I. K.; Enemark, J. H.; Kirk, M. L. *Inorg. Chem.* **1999**, *38*, 1401. (Note that following their definition of $C_s^{(XZ)}$ symmetry with the mirror plane bisecting the equatorial metal−ligand bonds, this paper makes an incorrect notational assignment of the *A*′ and *A*″ metal orbitals, including a d_{XY}-based instead of $d_{X^2-Y^2}$-based ground state.)
(32) Sproules, S. A.; Morgan, H. T.; Doonan, C. J.; White, J. M.; Young, C. G. *Dalton Trans.* **2005**, 3552.
(33) Collison, D.; Eardley, D. R.; Mabbs, F. E.; Rigby, K.; Bruck, M. A.; Enemark, J. H.; Wexler, P. A. *J. Chem. Soc., Dalton Trans.* **1994**, 1003.
(34) Nipales, N. S.; Westmoreland, T. D. *Inorg. Chem.* **1997**, *36*, 756.
(35) Peariso, K.; Chohan, B. S.; Carrano, C. J.; Kirk, M. L. *Inorg. Chem.* **2003**, *42*, 6194.
(36) Wilson, G. L.; Kony, M.; Tiekink, E. R. T.; Pilbrow, J. R.; Spence, J. T.; Wedd, A. G. *J. Am. Chem. Soc.* **1988**, *110*, 6923.
(37) Barnard, K. R.; Bruck, M.; Huber, S.; Grittini, C.; Enemark, J. H.; Gable, R. W.; Wedd, A. G. *Inorg. Chem.* **1997**, *36*, 637.
(38) McNaughton, R. L.; Helton, M. E.; Cosper, M. M.; Enemark, J. H.; Kirk, M. L. *Inorg. Chem.* **2004**, *43*, 1625.
(39) Cosper, M. M.; Neese, F.; Astashkin, A. V.; Carducci, M. D.; Raitsimring, A. M.; Enemark, J. H. *Inorg. Chem.* **2005**, *44*, 1290.
(40) Peng, G.; Nichols, J.; McCullough, E. A., Jr.; Spence, J. T. *Inorg. Chem.* **1994**, *33*, 2857.
(41) Young, C. G.; Enemark, J. H.; Collison, D.; Mabbs, F. E. *Inorg. Chem.* **1987**, *26*, 2925.
(42) Backes, G.; Enemark, J. H.; Loehr, T. M. *Inorg. Chem.* **1991**, *30*, 1839.
(43) Singh, R.; Spence, J. T.; George, G. N.; Cramer, S. P. *Inorg. Chem.* **1989**, *28*, 8.
(44) Young, C. G.; Gable, R. W.; Hill, J. P.; George, G. N. *Eur. J. Inorg. Chem.* **2001**, 2227.
(45) Young, C. G.; Laughlin, L. J.; Colmanet, S.; Scrofani, S. D. *Inorg. Chem.* **1996**, *35*, 5368.

Table 1. Selected Spectral Data for Tp*MoEX$_2$ (E = O, S) Complexes

compound	IR[a] ν(Mo≡E), cm^{-1}	near-IR[b] E, cm^{-1} (ϵ, M^{-1} cm^{-1})	UV−visible E, cm^{-1} (ϵ, M^{-1} cm^{-1})
Tp*MoS(etp)$_2$	500	7690 (87)	21550 (3520sh), 28250 (5920sh)
Tp*MoO(etp)$_2$	949	*g*	12500 (80), 19230 (1800sh)
Tp*MoS(pp)$_2$	497	7520 (110)	19610 (4430sh), 25130 (8600)
Tp*MoO(pp)$_2$	949	*g*	12500 (125sh), 18870 (2220)
Tp*MoS(OPh)$_2$	490	7520 (90)	20000 (3640sh), 26670 (8790)
Tp*MoO(OPh)$_2$[c]	949	*g*	13330 (80), 20830 (1440sh)
Tp*MoS(cat)	503	*g*	18050 (1800), 22990 (2660sh)
Tp*MoO(cat)[d,f]	940	*g*	15110 (190), 25380 (2400sh), 29410 (3400sh), 33220 (5500sh), 36500 (13600)
Tp*MoS(bdt)	500	*g*	20000 (3670sh), 21280 (4180), 32260 (7860)
Tp*MoO(bdt)[e]	932	9100 (360), 13100 (270)	19400 (270)
Tp*MoS(tdt)	490	*g*	19800 (4410sh), 21050 (4950), 32260 (9200)
Tp*MoO(tdt)[e,f]	926	9100 (490), 13000 (270)	19600 (1320sh)

[a] As KBr disks. [b] In dichloromethane; sh = shoulder. [c] Reference 51; in 1,2-$C_2H_4Cl_2$ solution. [d] Reference 49. [e] Reference 31. [f] Less recent data (in 1,2-$C_2H_4Cl_2$ solution) also appears in ref 51. [g] No features observed.

Chart 1. Ligand Structures

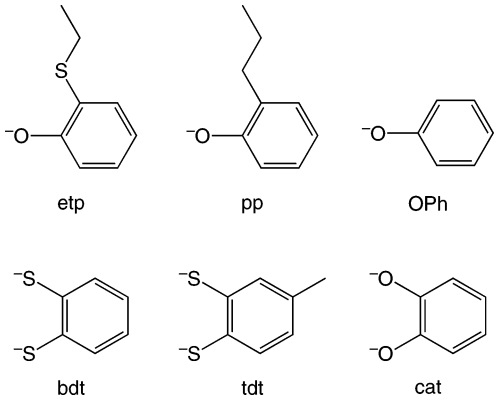

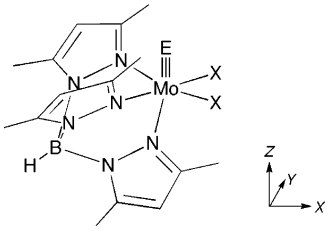

Figure 1. Structure of the Tp*MoEX$_2$ (E = O, S; X = etp, pp, OPh; X$_2$ = bdt, tdt, cat). The molecular symmetry axes are labeled (*X*,*Y*,*Z*), with the *Z* axis defined along the Mo≡E bond and the *X* axis bisecting the equatorial X ligating atoms. Lowercase *x*, *y*, *z* and *x*′, *y*′, *z*′ are used to designate the principal axes of **g** and **A**, respectively.

complex exhibits a distorted tetrahedral structure with an Mo≡S distance of 2.1677(12) Å.[46]

We report here full details of the synthesis and characterization of members of the first extended series of mononuclear thiomolybdenyl complexes, Tp*MoSX$_2$ [X = 2-(ethylthio)phenolate (etp), 2-(*n*-propyl)phenolate (pp), phenolate; X$_2$ = benzene-1,2-dithiolate (bdt), 4-methylbenzene-1,2-dithiolate (tdt), benzene-1,2-diolate (catecholate = cat) (see Chart 1 for structures of ligands)], Figure 1. The crystal structures of Tp*MoS(etp)$_2$, Tp*MoS(pp)$_2$, Tp*MoS(bdt), Tp*MoS(cat), and the molybdenyl complex, Tp*MoO(pp)$_2$, are also reported. Leading results have been communicated.[44] Multifrequency EPR studies of the complexes and associated spectral simulations and computational studies[47] have now been performed, allowing detailed analysis of the electronic structure. These reveal lower *g*-values for the thiomolybdenyl complexes compared with their molybdenyl analogues but have comparable **A**(^{95,97}Mo) values. The large noncoincidence of **g** and **A** indicates substantial configurational mixing in C_s or lower symmetry and contrasts with previously studied Tp*MoO(bdt)[48] and Tp*MoO(cat)[49] complexes whose X-band EPR spectra were simulated assuming orthorhombic symmetry.[49]

Experimental Section

Materials and General Methods. Potassium hydrotris(3,5-dimethylpyrazol-1-yl)borate,[50] Tp*MoOCl$_2$,[51] and Tp*MoSCl$_2$[41] were prepared according to literature procedures. The molybdenyl derivatives, Tp*MoO(etp)$_2$, Tp*MoO(pp)$_2$, Tp*MoO(bdt), and Tp*MoO(cat), were prepared according to literature methods or adaptions thereof.[51] The complexes were characterized by IR, EPR, and UV−vis spectroscopy (Tables 1 and 5), the results being consistent with literature reports. All reactions, purification procedures, and spectroscopic studies were performed under an atmosphere of dinitrogen using dried, deoxygenated solvents and reagents and standard Schlenk and glovebox techniques. Reactions were monitored by EPR spectroscopy and worked up when product formation was complete. Chromatographic separations and purifications were performed using Merck Art 7734 Kieselgel 60. Mass spectra were obtained on a JEOL JMS−AX505H mass spectrometer. Infrared spectra were recorded on a BIO−RAD FTS−165 FTIR spectrophotometer as pressed KBr discs. Electronic spectra were obtained on a Hitachi 150−20 spectrophotometer. Electrochemical experiments were performed using a Cypress Electrochemical System II with a 3 mm glassy carbon electrode and platinum auxiliary and reference electrodes. Solutions of Tp*MoSX$_2$

(46) Johnson, A. R.; Davis, W. M.; Cummins, C. C.; Serron, S.; Nolan, S. P.; Musaev, D. G.; Morokuma, K. *J. Am. Chem. Soc.* **1998**, *120*, 2071.
(47) Drew, S. C.; Young, C. G.; Hanson, G. R. *Inorg. Chem.* **2007**, *46*, 2388.
(48) Dhawan, I. K.; Enemark, J. H. *Inorg. Chem.* **1996**, *35*, 4873.
(49) Basu, P.; Bruck, M. A.; Li, Z.; Dhawan, I. K.; Enemark, J. H. *Inorg. Chem.* **1995**, *34*, 405.
(50) Trofimenko, S. *J. Am. Chem. Soc.* **1967**, *89*, 6288.
(51) Cleland, W. E., Jr.; Barnhart, K. M.; Yamanouchi, K.; Collison, D.; Mabbs, F. E.; Ortega, R. B.; Enemark, J. H. *Inorg. Chem.* **1987**, *26*, 1017.

Table 2. X-ray Crystallographic Data

compound	Tp*MoS(etp)	Tp*MoS(pp)$_2$	Tp*MoO(etp)$_2$	Tp*MoS(bdt)	Tp*MoS(cat)
formula	$C_{31}H_{40}BMoN_6O_2S_3$	$C_{33}H_{44}BMoN_6O_2S$	$C_{31}H_{40}BMoN_6O_3S_2$	$C_{21}H_{26}BMoN_6S_3$	$C_{21}H_{26}BMoN_6O_2S$
fw	731.65	695.57	715.58	565.42	533.29
space group	$P\bar{1}$	$P2_1/c$	$P\bar{1}$	$P2_1/n$	*Pbca*
a, Å	10.825(2)	14.0547(12)	10.8664(15)	10.0296(13)	14.167(3)
b, Å	11.584(2)	10.085(2)	11.4769(15)	14.729(2)	18.890(5)
c, Å	14.428(2)	24.747(4)	15.069(2)	16.846(2)	17.547(4)
α, deg	86.735(11)	90	102.347(10)	90	90
β, deg	88.669(12)	90.183(9)	96.032(10)	95.456(10)	90
γ, deg	71.998(13)	90	110.426(10)	90	90
V, Å^3	1717.8(5)	3507.7(9)	1686.9(4)	2477.3(6)	4695.8(19)
Z	2	4	2	4	8
ρ_{calc}, g·cm^{-3}	1.414	1.317	1.409	1.516	1.509
R^a	0.0390	0.0310	0.0324	0.0346	0.0889
$R_w{}^b$	0.0998	0.0862	0.0782	0.0967	0.2744

^{a} $R[I>2\sigma(I)] = s||F_o| - |F_c|\Sigma/\Sigma|F_o|$. ^{b} R_w[all data] $= [\Sigma w(F_o^2 - F_c^2)^2/\Sigma w(F_o)^2]^{1/2}$.

Table 3. Selected Bond Distances (Å) and Angles (deg) for Tp*MoE(etp)$_2$ (E = O, S) and Tp*MoS(pp)$_2$

distance/angle	Tp*MoS(etp)$_2$	Tp*MoS(pp)$_2$	Tp*MoO(etp)$_2$
Mo−E(1)	2.1280(11)	2.1368(8)	1.675(2)
Mo−O(4)	1.953(2)	1.952(2)	1.953(2)
Mo−O(5)	1.951(2)	1.946(2)	1.951(2)
Mo−N(11)	2.278(3)	2.282(2)	2.285(2)
Mo−N(21)	2.174(3)	2.195(2)	2.181(2)
Mo−N(31)	2.175(3)	2.183(2)	2.179(2)
E(1)−Mo−O(4)	104.20(8)	101.25(6)	104.90(9)
E(1)−Mo−O(5)	101.10(7)	103.70(6)	100.91(9)
E(1)−Mo−N(11)	168.28(7)	168.11(5)	165.53(9)
E(1)−Mo−N(21)	91.00(8)	91.83(6)	89.20(9)
E(1)−Mo−N(31)	92.82(8)	91.64(6)	91.74(9)
O(4)−Mo−O(5)	89.95(9)	91.09(7)	90.15(8)
O(4)−Mo−N(11)	86.10(10)	85.72(7)	87.90(8)
O(4)−Mo−N(21)	164.75(10)	165.78(7)	165.84(8)
O(4)−Mo−N(31)	90.41(10)	86.62(7)	91.74(8)
O(5)−Mo−N(11)	84.23(9)	85.63(7)	85.50(8)
O(5)−Mo−N(21)	88.35(10)	91.20(7)	88.51(8)
O(5)−Mo−N(31)	165.54(9)	164.64(8)	166.27(8)
N(11)−Mo−N(21)	78.65(10)	80.46(7)	77.93(8)
N(11)−Mo−N(31)	81.38(10)	79.06(7)	80.98(8)
N(21)−Mo−N(31)	87.51(10)	87.46(7)	86.34(8)
Mo−O(4)−C(41)	140.9(2)	134.6(2)	139.2(2)
Mo−O(5)−C(51)	134.4(2)	143.8(2)	134.3(2)

Table 4. Selected Bond Distances (Å) and Angles (deg) for Tp*MoS(bdt) and Tp*MoS(cat)

distance/angle	Tp*MoS(bdt)	Tp*MoS(cat)
Mo−S(1)	2.1232(11)	2.134(3)
Mo−E(4)	2.3704(12)	1.997(4)
Mo−E(5)	2.3668(12)	1.977(4)
Mo−N(11)	2.393(3)	2.361(5)
Mo−N(21)	2.201(3)	2.157(5)
Mo−N(31)	2.189(3)	2.159(6)
S(1)−Mo−E(4)	101.24(5)	100.6(2)
S(1)−Mo−E(5)	100.99(5)	101.8(2)
S(1)−Mo−N(11)	168.93(8)	168.1(2)
S(1)−Mo−N(21)	92.88(9)	92.0(2)
S(1)−Mo−N(31)	95.09(9)	93.6(2)
E(4)−Mo−E(5)	83.84(4)	79.6(2)
E(4)−Mo−N(11)	86.34(8)	87.9(2)
E(4)−Mo−N(21)	91.14(9)	94.6(2)
E(4)−Mo−N(31)	163.58(9)	165.2(2)
E(5)−Mo−N(11)	87.76(9)	87.8(2)
E(5)−Mo−N(21)	165.92(9)	165.8(2)
E(5)−Mo−N(31)	91.40(9)	93.6(2)
N(11)−Mo−N(21)	78.78(12)	80.0(2)
N(11)−Mo−N(31)	77.76(11)	78.7(2)
N(21)−Mo−N(31)	89.77(11)	88.9(2)
Mo−E(4)−C(41)	104.11(14)	112.1(4)
Mo−E(5)−C(42)	104.21(14)	112.6(4)

(1−2 mM) in dry, deoxygenated 0.1 M NBu$^n{}_4$BF$_4$/acetonitrile were employed, and potentials were referenced to internal ferrocene (+0.390 V vs saturated calomel electrode (SCE)). Potentials are reported relative to the SCE. Microanalyses were performed by Atlantic Microlabs, Norcross, GA. Selected spectral data are presented in Table 1.

Syntheses. Tp*MoS(etp)$_2$. 2-Ethylthiophenol (0.18 mL, 1.01 mmol) and triethylamine (0.15 mL, 1.01 mmol) were added to a stirred solution of Tp*MoSCl$_2$ (250 mg, 0.5 mmol) in dichloromethane (30 mL). The solution rapidly turned purple and then became brown in color. After 4 h of stirring, the volume of the solution was reduced to a minimum (~10 mL) and then filtered through a 4−5 × 2 cm diameter bed of silica gel. The silica was washed with dichloromethane (30 mL), and the combined filtrate and washings were reduced to a minimum volume and treated (dropwise) with methanol. The red crystals were filtered, washed with methanol, and vacuum-dried. Yield 150 mg (41%).

Anal. Calcd $C_{31}H_{40}BMoN_6O_2S_3$: C, 50.89; H, 5.51; N, 11.49; S, 13.15. Found: C, 51.06; H, 5.27; N, 11.69; S, 13.30. IR (KBr): ν(BH) 2525m, 1570m, ν(CN) 1541s, 1459s, 1364s, 1261s, 1201s, 1068s, 857s, 748s, 693s, 615s, ν(MoS) 500s cm^{-1}. Mass spec: *m*/*z* [M − H]$^+$ 732.

Tp*MoS(pp)$_2$. 2-Propylphenol (110 mg, 0.80 mmol) and triethylamine (0.12 mL, 0.80 mmol) were added to a stirred solution of Tp*MoSCl$_2$ (200 mg, 0.40 mmol) in dichloromethane (30 mL). The solution rapidly turned purple and then became brown in color. The reactions was worked up as described above for Tp*MoS(etp)$_2$. The yield of red crystals was 120 mg (43%).

Anal. Calcd for $C_{33}H_{44}BMoN_6O_2S$·0.2CH_2Cl_2: C, 55.96; H, 6.28; N, 11.79; S, 4.50; Cl, 1.99. Found: C, 55.83; H, 6.50; N, 12.05; S, 4.44; Cl, 2.03. IR (KBr): ν(BH) 2551m, 1590m, ν(CN) 1543s, 1467s, 1447s, 1416s, 1383s, 1364s, 1234s, 1204s, 1187m, 1121m, 1070s, 1046s, 898m, 859s, 811m, 786s, 751s, 692m, 650m, 623m, ν(MoS) 497s cm^{-1}. Mass spec: *m*/*z* [M − H]$^+$ 695.

Tp*MoS(bdt). 1,2-Benzenedithiol (0.1 mL, 0.90 mmol) and triethylamine (0.29 mL, 1.90 mmol) were added to a stirred solution of Tp*MoSCl$_2$ (450 mg, 0.90 mmol) in dichloromethane (30 mL). The solution rapidly turned a red color, and after 2 h the reaction was worked up as described above for Tp*MoS(etp)$_2$. The yield of red crystals was 220 mg (43%). The analytical sample was purified by anaerobic column chromatography on silica gel using 3:2 dichloromethane:hexane as eluent and then recrystallized from dichloromethane/methanol.

Anal. Calcd for $C_{21}H_{26}BMoN_6S_3$·0.5CH_3OH: C, 44.41; H, 4.85; N, 14.45; S, 16.54. Found: C, 44.02; H, 4.77; N, 14.40; S 16.49. IR (KBr): ν(BH) 2557m, ν(CN) 1540s, 1447s, 1435s, 1412s, 1357s,

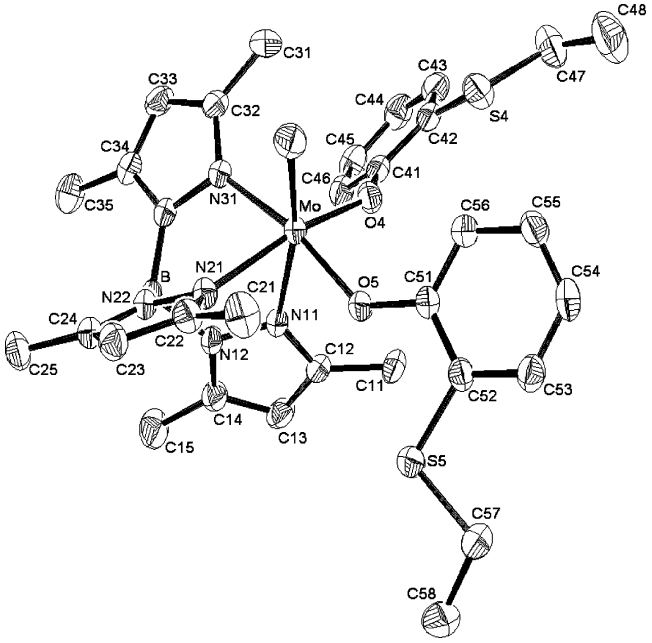

Figure 2. X-ray crystallographic structure of Tp*MoS(etp)$_2$, drawn with 30% probability ellipsoids.

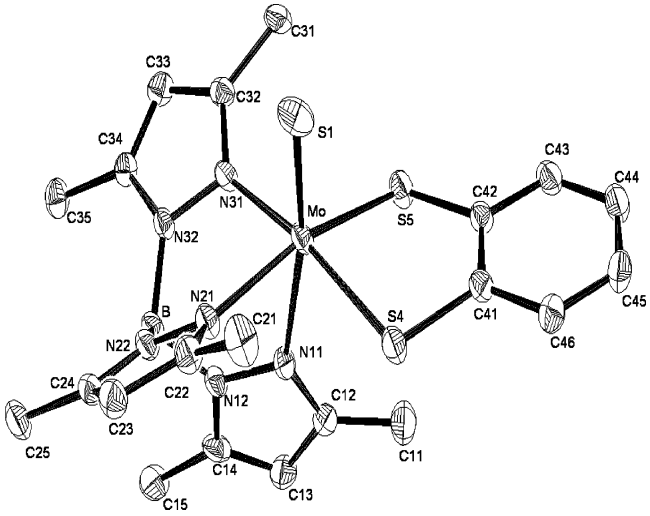

Figure 3. X-ray crystallographic structure of Tp*MoS(bdt), drawn with 30% probability ellipsoids.

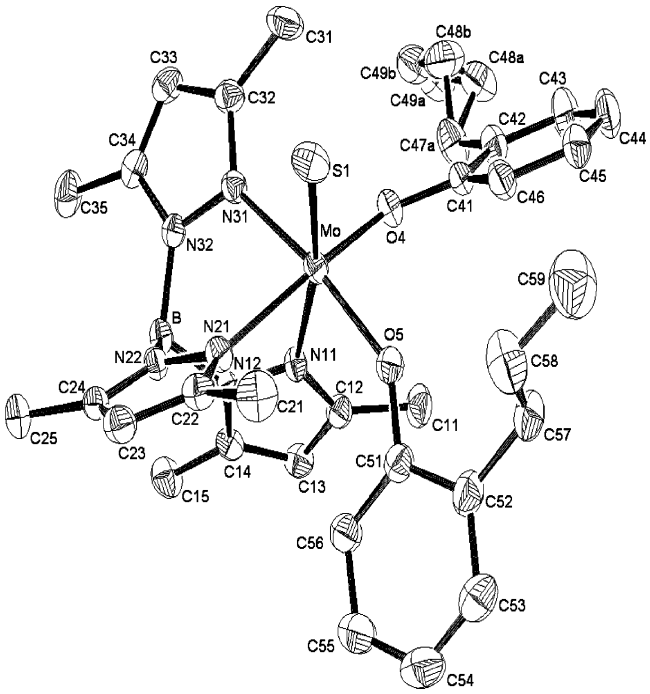

Figure 4. X-ray crystallographic structure of Tp*MoS(pp)$_2$ drawn with 30% probability ellipsoids. Both positions for the disordered propyl group on C(42) are shown.

1262m, 1202s, 1093m, 1074s, 1036s, 854m, 814m, 790s, 745s, 692m, 666w, 647w, ν(MoS) 499s cm^{-1}. Mass spec: *m*/*z* [M − H]$^+$ 568.

Tp*MoS(cat). Triethylamine (0.12 mL, 0.8 mmol) was added to a stirred mixture of Tp*MoSCl$_2$ (200 mg, 0.4 mmol) and catechol (44 mg, 0.4 mmol) in dichloromethane (30 mL). The solution rapidly turned a brown color, and after 2 h the reaction was worked up as described above for Tp*MoS(etp)$_2$. The yield of brown crystals was 120 mg (56%).

Anal. Calcd for $C_{21}H_{26}BMoN_6O_2S$: C, 47.29; H, 4.91; N, 15.76; S, 6.01. Found: C, 47.19; H, 5.03; N, 15.59; S, 5.89. IR (KBr): ν(BH) 2554m, ν(CN) 1542s, 1451s, 1416s, 1386m, 1364s, 1262m, 1241s, 1203s, 1100s, 1078s, 1017s, 910w, 858m, 797s, 737s, 693m, 647s, 616m, 530m, ν(MoS) 503s, 472w cm^{-1}. Mass spec: *m*/*z* [M]$^+$ 536.

Tp*MoS(tdt). Triethylamine (0.12 mL, 0.80 mmol) was added to a stirred mixture of Tp*MoSCl$_2$ (200 mg, 0.4 mmol) and 3,4-toluenedithiol (70 mg, 0.44 mmol) in dichloromethane (30 mL). The solution rapidly turned a deep red color, and after 3 h the reaction was worked up as described above for Tp*MoS(etp)$_2$. The yield of red crystals was 100 mg (43%).

Anal. Calcd for $C_{22}H_{28}BMoN_6OS_3$: C, 45.60; H, 4.87; N, 14.50; S, 16.60. Found: C, 45.34; H, 4.60; N, 14.63; S, 16.45. IR (KBr): ν(BH) 2554m, ν(CN) 1541s, 1447s, 1412s, 1356s, 1261s, 1200s, 1096s, 1033s, 853m, 801s, 688w, 650w, ν(MoS) 490m cm^{-1}. Mass spec: *m*/*z* [M]$^+$ 580.

Tp*MoS(OPh)$_2$.. Triethylamine (0.29 mL, 1.9 mmol) was added to a stirred mixture of Tp*MoSCl$_2$ (450 mg, 0.90 mmol) and phenol (170 mg, 1.9 mmol) in dichloromethane (30 mL). The solution rapidly turned a red/brown color, and after 2 h the reaction was worked up as described above for Tp*MoS(etp)$_2$. The yield of red crystals was 200 mg (36%).

Anal. Calcd for $C_{27}H_{32}BMoN_6O_2S$: C, 53.04; H, 5.28; N, 13.75; S, 5.24. Found: C, 52.86; H, 5.03; N, 13.68; S, 5.29. IR (KBr): ν(BH) 2541m, 1582s, ν(CN) 1534s, 1473s, 1443s, 1416s, 1362s, 1275m, 1254s, 1200s, 1163m, 1064m, 1010m, 872s, 845s, 802s, 742s, 683s, 629s, 598m, ν(MoS) 490s cm^{-1}. Mass spec: *m*/*z* [M − H]$^+$ 612.

Crystal Structures. Crystals of Tp*MoS(etp)$_2$ and Tp*MoS(bdt) were grown by slow diffusion of methanol into dichloromethane solutions of the compounds. Crystals of Tp*MoO(etp)$_2$ were obtained by slow evaporation from dichloromethane and those of Tp*MoS(pp)$_2$ and Tp*MoS(cat) by slow evaporation from dichloromethane/methanol mixtures. Crystallographic data (CIFs, Supporting Information, and ref 44) are summarized in Table 2. Data were collected using an Enraf-Nonius CAD4-MachS single-crystal diffractometer using the ω:2θ scan method with graphite monochromated Mo Kα radiation (λ = 0.71073 Å) at 293 K. Cell parameters were obtained by a least-squares procedure from the angular settings of 25 carefully centered reflections. All five structures were solved by Patterson and direct methods (SHELXS−86)[52] and were refined on F^2 by a full-matrix least-squares procedure (SHELXL−97),[53] with anisotropic displacement parameters assigned to all atoms and using all data. All

H-atoms were included at geometrical estimates. For Tp*MoO(etp)$_2$ the ethyl group attached to S(4) and for Tp*MoS(pp)$_2$ the propyl group attached to C(42) were found to be disordered (Figure 4). Refinements were carried out with these atoms distributed over two positions, with each atom assigned an individual temperature factor and with both components restrained to have similar geometry; the final occupancy factors were 0.523(7) and 0.477(7) and 0.65(1) and 0.35(1), respectively. The structure of Tp*MoS(bdt) showed evidence of minor disorder, but only the Mo atom of the second component could be reliably included in the refinement; the final occupancy factors were 0.974(2) and 0.026(2). The structure of Tp*MoS(cat) was also found to be disordered, and refinement was carried out with the molecule distributed over five positions, with isotropic displacement parameters assigned to nearly all of the atoms of the four minor components. No H-atoms were found in the difference maps, and none were included in the refinement. During the refinement all five components were constrained to have similar geometrical parameters; the final occupancy factors were 0.522(3), 0.125(6), 0.084(5), 0.138(7), and 0.132(8), respectively. Selected bond distances and angles in the complexes containing only monodentate coligands are presented in Table 3; those pertaining to the bidentate complexes are given in Table 4. Figures 2−4 were drawn from the output of ORTEP.[54] CIFs for Tp*MoS(bdt) and Tp*MoS(etp)$_2$ (CCDC-157193 and -157194) are available elsewhere.[44]

EPR Spectroscopy. Multifrequency (Q-, X- and S-band) continuous wave EPR spectra of 1 mM chloroform solutions of the complexes were recorded on a Bruker Biospin Elexsys E500 EPR spectrometer fitted with either a cylindrical cavity (Q-band), rectangular cavity (X-band), or flexline (S-band) resonator. Calibration of the magnetic field and microwave frequency were achieved with a Bruker ER 035M Gaussmeter and an EIP 548B microwave frequency counter, respectively. A flow-through cryostat in conjunction with a Eurotherm (B-VT-2000) variable temperature controller provided temperatures of 120−140 K at the sample position in the cavity. Spectrometer tuning, signal averaging, and subsequent spectral comparisons were performed with Bruker's Xepr (version 2.1) software. High quality figures presented herein were generated using gnuplot.[55]

Computer simulations of the EPR spectra were performed using version 1.1.4 of the XSophe-Sophe-XperView computer simulation software suite running on a personal computer with the Mandrake Linux v9.1 operating system. The computational program, SOPHE, employs a number of methods, including matrix diagonalization, SOPHE interpolation, and homotopy for the analysis of randomly oriented EPR spectra. In this research we employed matrix diagonalization in conjunction with mosaic misorientation[56] to simulate the randomly oriented EPR spectra from the Mo(V) complexes, which significantly reduces the computational times. A distribution of principal *g* and *A* values was employed to account for the line width variation in the anisotropic spectra. Comparisons of simulated and experimental spectra and data manipulation were performed with Xepr.

The simulations used a spin Hamiltonian of the form

$$H = \beta_e \mathbf{B}\cdot\mathbf{g}\cdot\mathbf{S} + \sum_{I=0,5/2} (\mathbf{S}\cdot\mathbf{A}\cdot\mathbf{I} - \gamma_n \mathbf{B}\cdot\mathbf{I}) \qquad (1)$$

where the weighted summation is over all naturally occurring isotopes (^{90,92,94,96,98,100}Mo, $I = 0$, 74.53% abundant; ^{95}Mo, $I = 5/2$, $\mu = -0.9142$, 15.92% abundant; ^{97}Mo, $I = 5/2$, $\mu = -0.9335$, 9.55% abundant), β_e is the Bohr magneton, **B** is the static magnetic field, **g** and **A** are the 3×3 electron Zeeman and ^{95,97}Mo hyperfine interaction matrices, respectively, **S** and **I** are the electron and nuclear spin vector operators, respectively, and γ_n is the gyromagnetic ratio of the $I = 5/2$ ^{95,97}Mo nuclei. Monoclinic spin Hamiltonian parameters were able to be fitted to all multifrequency EPR spectra; it was not possible to unambiguously fit a lower symmetry spin Hamiltonian to the spectra of the triclinic complexes.

In monoclinic (C_{2h}, C_2, C_s) symmetry, **g** and **A** have only one principal axis in common. For the geometry in Figure 1, we have $C_s^{(XZ)}$ symmetry, and g_{yy} and $A_{y'y'}$ are coaxial and normal to the Mo≡E (E = O, S) bond axis (the molecular *Z* axis). In the randomly oriented EPR spectrum, when the magnetic field is directed along the canonical directions of **g**, the first-order hyperfine splitting *A* is given by[57]

$$A^2 = \begin{cases} A_{x'x'}{}^2 \cos^2\beta + A_{z'z'}{}^2 \sin^2\beta, & \mathbf{B} \,||\, \hat{x} \\ A_{x'x'}{}^2 \sin^2\beta + A_{z'z'}{}^2 \cos^2\beta, & \mathbf{B} \,||\, \hat{z} \end{cases} \qquad (2)$$

where (x,y,z) and (x',y',z') are the principal axis systems of **g** and **A**, respectively, and β is a component of a general Euler rotation $R(\alpha,\beta,\gamma) = R_z(\gamma)R_y(\beta)R_z(\alpha)$ transforming the principal axes of **A** to those of **g**. The isotropic hyperfine splitting (A_{iso}) obtained from the room-temperature spectra (not shown) was used as a guide to fitting the anisotropic spin Hamiltonian parameters in the frozen solution spectra.[58]

Results and Discussion

Synthesis and Characterization. The reactions of Tp*MoOX$_2$ with boron sulfide in dichloromethane resulted in *in situ* generation of Tp*MoSX$_2$ according to EPR spectroscopy; however, only impure products could be isolated from these reactions. In contrast, metathetical reactions, of Tp*MoSCl$_2$ with HX or H_2X_2 and NEt$_3$ in dichloromethane, produced isolable Tp*MoSX$_2$ (X = OPh, etp, pp; X_2 = cat, tdt, bdt) complexes. These reactions were conveniently monitored by EPR spectroscopy, which revealed the clean replacement of Tp*MoSCl$_2$ by product over a period of 2−16 h. Rapid, anaerobic workup, including passage through a short bed of silica gel, was essential to the isolation of products. Chromatographic purifications, recrystallizations, and spectroscopic studies were performed under strictly anaerobic conditions. The compounds are air-stable for several days in the solid state but rapidly decompose in air in solution. The stability of the thiomo-

(52) Sheldrick, G. M. SHELXS-86, Program for Crystal Structure Solution. *Acta Crystallogr., Sect. A: Found. Crystallogr*. **1990**, *A46*, 467.
(53) Sheldrick, G. M. *SHELXL-97. Program for Crystal Structure Refinement*, University of Göttingen: Germany, 1997.
(54) Johnson, C. K. *ORTEPII*; Report ORNL-5138; Oak Ridge National Laboratory: Oak Ridge, TN, 1976. Farrugia, L. J. ORTEP-3 for Windows, v1.08. *J. Appl. Crystallogr*. **1997**, *30*, 565.
(55) Gnuplot maybe obtained from www.gnuplot.info.
(56) Hanson, G. R.; Gates, K. E.; Noble, C. J.; Griffin, M.; Mitchell, A.; Benson, S. *J. Inorg. Biochem*. **2004**, *98*, 903.
(57) Pilbrow, J. R.; Winfield, M. E. *Mol. Phys.* **1973**, *25*, 1073.
(58) It was assumed that any effects due to a change of molecular environment upon freezing or due to the influence of the asymmetry in **A** (Pilbrow, J. R. *Transition Ion Electron Paramagnetic Resonance*; Clarendon Press: Oxford, 1990; §3.7 and §5.3.4. Belford, R. L.; Pilbrow, J. R. *J. Magn. Reson.* **1973**, *11*, 381.) were of a similar magnitude to the overall uncertainty in the EPR simulations.

lybdenyl complexes appears to be enhanced by very bulky, oxygen donor coligands such as etp and pp or chelating ligands such as tdt and bdt.

The complexes were characterized by microanalysis, mass spectrometry, spectroscopy, and X-ray crystallography. IR spectra exhibited a single, strong ν(Mo≡S) band in the range 505−490 cm^{-1} as well as bands characteristic of Tp* (ν(BH) ∼ 2550 cm^{-1} and ν(CN) ∼ 1540 cm^{-1}) and the O- or S-donor coligands. Bands in the range 530−470 cm^{-1} are characteristic of terminal sulfido complexes.[59] Oxo analogues exhibit ν(Mo≡O) bands around 940−910 cm^{-1}.

Referring to Table 1, the sulfido complexes containing monodentate O-donor ligands exhibit a low-energy d−d transition in the near-IR region at 7500−7700 cm^{-1} (ϵ ∼ 100 M^{-1} cm^{-1}) and more intense charge-transfer transitions above 19 000 cm^{-1} (ϵ > 3000 M^{-1} cm^{-1}). The related d−d transitions of analogous oxo complexes are higher in energy at ∼13 000 cm^{-1}. Similar features are observed in the spectra of Tp*MoECl$_2$, where the d−d bands have been assigned to transitions from the Mo $d_{X^2-Y^2}$ ground-state orbital (S(H)-OMO = singly (highest) occupied molecular orbital) to Mo d_{YZ} and/or d_{XZ} orbitals.[41] The relatively low energy of the d−d transition in the sulfido complexes reflects the smaller SOMO−LUMO (LUMO = lowest unoccupied molecular orbital) gap associated with the weaker π-base sulfido ligand compared with the strong π-base oxo ligand. The lowest energy bands of sulfido complexes containing bidentate benzenoid ligands occur at >18 000 cm^{-1} and possess considerable charge-transfer character (ϵ >1800 M^{-1} cm^{-1}). In contrast, relatively weak bands (ϵ ∼ 300−500 M^{-1} cm^{-1}) in the near-IR have been observed in oxo complexes containing bdt and tdt ligands. Comparing the monodentate complexes with the bidentate complexes, the former exhibit d−d transitions in the near-IR while the latter do not, indicating that the HOMO−LUMO gap in the monodentate Tp*MoE(OR)$_2$ complexes is lower.

Electrochemistry. The complexes can be divided into two classes based on their electrochemical behavior. The bidentate sulfur−donor ligand complexes constitute a small group with exceptionally high reversible reduction potentials, $E_{1/2}$, of −271 mV and −300 mV for Tp*MoS(bdt) and Tp*MoO-(tdt), respectively. The other compounds are reduced at more negative potentials. The oxygen−donor ligand complexes are reduced at much more negative potentials. For example, Tp*MoS(pp)$_2$ and Tp*MoS(cat) exhibit reversible reductions at −950 mV and −825 mV, respectively, while Tp*MoO-(etp)$_2$ displays evidence of two reversible cathodic processes at −690 mV and −900 mV. The compounds also exhibit irreversible oxidation waves at around +500 mV. The reversible cathodic processes are interpreted in terms of a reversible reduction of Mo(V) to Mo(IV).

Crystal Structures. The structures of Tp*MoS(etp)$_2$ (Figure 2), Tp*MoO(etp)$_2$ (Supporting Information), Tp*MoS-(bdt) (Figure 3), Tp*MoS(pp)$_2$ (Figure 4), and Tp*MoS(cat) (Supporting Information) have been determined by X-ray diffraction. Selected bond lengths and angles are presented in Tables 3 and 4. The mononuclear, six-coordinate complexes exhibit distorted octahedral coordination geometries. The coordination sphere is comprised of terminal sulfido, tridentate Tp*, and monodentate (X) or bidentate (X_2) ligands. The terminal sulfido and X/X_2 ligands are mutually *cis* as a result of the *facial* coordination of the Tp* ligand. The molybdenum atom lies out of the equatorial plane toward the sulfido ligand resulting in S−Mo−N/X angles around 100° and a lengthening of the Mo−N bond *trans* to the sulfido ligand.

For Tp*MoS(etp)$_2$ and Tp*MoS(pp)$_2$ (parameters for the latter in square brackets), the largest deviations from an octahedral geometry are in the S(1)−Mo−O(4/5) (av 102.7° [102.5°]), S(1)−Mo−N(11) (168.27(7)° [168.11(5)°]), and O(4/5)−Mo−N(21/31) (av 165.2° [165.2°]) angles. The latter are a consequence of N−Mo−N angles of 78−88° typical of the Tp* ligand. Other angles within the coordination sphere deviate by less than 4° from ideal angles. The Mo atom lies 0.264(1) Å [0.259(1) Å] out of the O(4)/O(5)/N(21)/N(31) plane (max deviation = 0.009(1) Å [0.016(1) Å]) toward the sulfido ligand. The Mo−S(1) distance of 2.128(1) Å [2.1368(8) Å] is typical of terminal sulfido ligands in di/polynuclear Mo complexes but slightly shorter than the Mo≡S bond of 4-coordinate MoS(NRAr)$_3$ (2.1677-(12) Å). The *trans* influence of this ligand lengthens the Mo−N(11) bond to 2.278(3) Å [2.282(2) Å], 0.10 Å [0.09 Å] longer than the other Mo−N distances. The average Mo−O(4/5) distance of 1.952 Å [1.949 Å] is close to the medium value from other structures (1.956 Å), and the average Mo−O−C angle of 137.7° [139.2°] is typical of aryloxy ligands; the Mo−O−C angles can be ascribed to a degree of O sp^2 character π−bonding within the Mo≡O unit.

The molecules possess C_1 symmetry in the solid state by virtue of the arrangement of the phenoxide ligand substituents. The R-group of one ligand projects toward the sulfido ligand, while the other is directed away from this ligand. In Tp*MoS(etp)$_2$ the S(1)···S(4) distance of 4.538(2) Å is substantially larger than the sum of the van der Waals radii (3.7 Å) and indicates that a stabilizing S···S interaction is absent (consistent with the Mo−S(1) distance). In Tp*MoS(etp)$_2$, the atoms of the thioether substituents are nearly coplanar to the phenyl groups to which they are attached. This is not the case for Tp*MoS(pp)$_2$. However, in both cases, the bulk of the X ligands appears to provide a high degree of steric protection to the sulfido ligand. The oxo−Mo(V) complex, Tp*MoO(etp)$_2$, exhibits a structure similar to that of its sulfido analogue (Table 3). The Mo−O(1) distance of 1.675(2) Å is typical of oxo−Mo(V) species.

The complexes Tp*MoS(bdt) and Tp*MoS(cat) contain bidentate ligands. Here the S(1)−Mo−X angles are again greater than 100°, and the S(1)−Mo−N(11) angle is approximately 168°. The Mo−S(1) distances of 2.1231(11) and 2.134(3) Å, respectively, are typical of Mo≡S units. For Tp*MoS(bdt), the Mo−S(41) and Mo−S(42) distances of

(59) Young, C. G.; Roberts, S. A.; Ortega, R.; Enemark, J. H. *J. Am. Chem. Soc.* **1987**, *109*, 2938. Müller, A.; Diemann, E. In *Comprehensive Coordination Chemistry;* Wilkinson, G., Gillard, R. D., McCleverty, J. A., Eds.; Pergamon: Oxford, 1987; Chapter 16.1, pp 515−550. Parkin, G. *Prog. Inorg. Chem.* **1998**, *47*, 1.

2.370(1) Å and 2.367(1) Å are somewhat shorter than the mean in related structures (2.408 Å); associated Mo−S−C angles are 104.11(14)° and 104.21(14)°, respectively. The Mo atom lies 0.296 Å out of the plane defined by S(41)/S(42)/N(21)/N(31) toward the sulfido ligand. The Mo−N(11) distances are dictated by the relative *trans* influences of the coligands, with the Mo−N(11) distance lengthened by ca. 0.20 Å relative to the other two Mo−N bonds. There are no apparent interactions between the terminal sulfido ligand and the sulfur donor atoms of bdt, the S···S distances (>4.5 Å) being considerably larger than the van der Waals contact distance. The oxo complex Tp*MoO(bdt) is isomorphous and isostructural to Tp*MoS(bdt), with Mo≡O and Mo−S_{av} distances of 1.678(4) Å and 2.373 Å, respectively.[48] With the exception of the terminal chalcogenide ligands, the metal and donor atoms of both molecules are virtually superimposable; a common Mo−E vector is also evident upon superposition of the molecules. The S(41) to S(42) distance is 3.17 Å.

It is interesting to note that in Tp*MoS(bdt) the bdt ligand is not coplanar with the Mo atom, the fold angle between the planes comprising Mo, S4, and S5, and S4, C41, C42, and S5 being 25.25(5)°; in Tp*MoS(cat) the corresponding angle is 21.1(4)°.

EPR Spectroscopy. The isotropic room temperature solution EPR spectra (not shown) of Tp*MoEX_2 (E = S, O; X = etp, pp, OPh; X_2 = cat, bdt, tdt) were measured at S- and X-band microwave frequencies and found to be typical of mononuclear Mo(V) species (d^1, S = 1/2) exhibiting a central resonance from[90,92,94,96,98,100] Mo (I = 0, 74.53% abundant) isotopes flanked by six hyperfine resonances from the [95,97]Mo, (I = 5/2, 25.47% abundant) isotopes.[60] Computer simulation of these spectra produced the isotropic g and A values listed in Table S1.

The frozen solution EPR spectra for all of the thiomolybdenyl complexes are highly anisotropic, and representative experimental and simulated EPR spectra of Tp*MoS(cat) and Tp*MoS(tdt) are shown in Figures 5 and 6, respectively. Representative spectra for Tp*MoO(cat), Tp*MoO(bdt), and Tp*MoO$(etp)_2$ are also shown in Figures 7−9, respectively. A comparison of the spin Hamiltonian parameters of Tp*MoEX_2 is given in Table 5. While Q-band EPR spectra provided superior g-value resolution, the S-band frozen solution spectra proved most sensitive to the [95,97]Mo hyperfine interaction due to enhanced second-order effects on the resonant field positions (arising from state mixing) and reduced g-A strain which produced narrower line widths. Q-band microwave frequencies were particularly useful for Tp*MoE(cat) (E = S, O) where at S- and X-band only axial g-values could be extracted, whereas the higher frequency was able to clearly resolve g_{xx} and g_{yy} (Figures 5 and 7).

Consistent with the low point group symmetry of the molecules, the resonant field positions arising from [95,97]Mo hyperfine coupling, especially the sextet due to the apparent

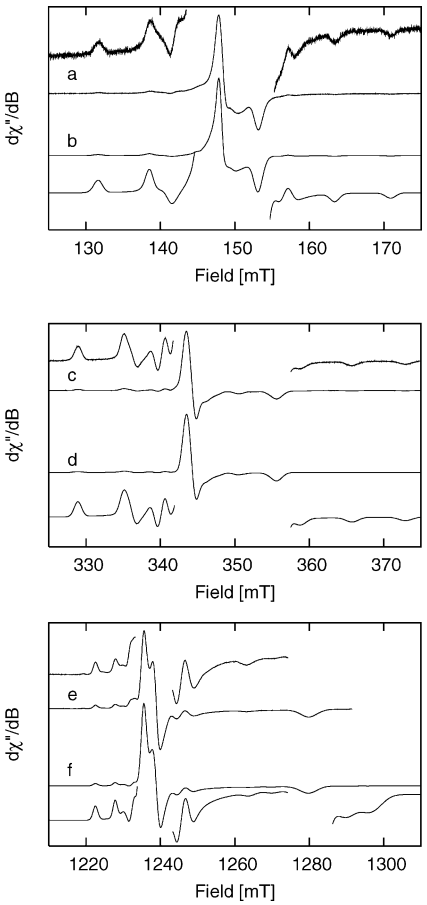

Figure 5. Multifrequency EPR spectra of Tp*MoS(cat) at 130 K. (a) S-band experimental spectrum, ν = 4.0618 GHz; (b) simulated S-band spectrum; (c) X-band experimental spectrum, ν = 9.4428 GHz; (d) simulated X-band spectrum; (e) Q-band experimental spectrum, ν = 33.948 GHz; and (f) simulated Q-band spectrum. (a,b) Insets expanded by 15 and 12.36, respectively; (c,d) insets expanded by 14 and 23.08, respectively; and (e,f) low field insets expanded by 3.63 and 6.25, respectively, and high field insets expanded by 5.38 and 6.25, respectively.

A_{zz} splitting (vide infra),[61] could not be successfully reproduced in the multifrequency spectral simulations without the introduction of at least one Euler angle (Table 5) to align the apparent center of these resonances. It is evident that this is not only just a property of the thiomolybdenyl complexes but also of the molybdenyl X = etp, pp complexes synthesized by us. In principle, the spin Hamiltonian of the triclinic molecules with monodentate donor ligands can additionally have nonzero α and γ Euler angles. However, variation of the third Euler angle γ had only a minimal influence on the spectral simulations, this being a direct consequence of the similar magnitude of $A_{x'x'}$ and $A_{y'y'}$. Likewise, we also found it difficult to conclusively fit a nonzero value of α due to limited spectral resolution. For Tp*MoS$(pp)_2$, for example, we could introduce α angles of up to 10° (in addition to the β = 25° rotation) without significant changes to the fit.

Very similar EPR parameters, with a notably low g_{zz} = 1.86 characterize the three available Tp*MoS$(OR)_2$ com-

(60) X-band EPR spectra of Tp*MoS$(OPh)_2$, Tp*MoS$(etp)_2$, and Tp*MoS(tdt) revealed the presence of an additional minor species (<4%) which may be attributed to unreacted starting material.

(61) To reiterate, we use the (x,y,z) coordinate system to identify the principal directions of the **g** matrix and (x',y',z') to identify those of the **A** matrix. The molecular coordinate system is defined by the X,Y,Z axes (Figure 1).

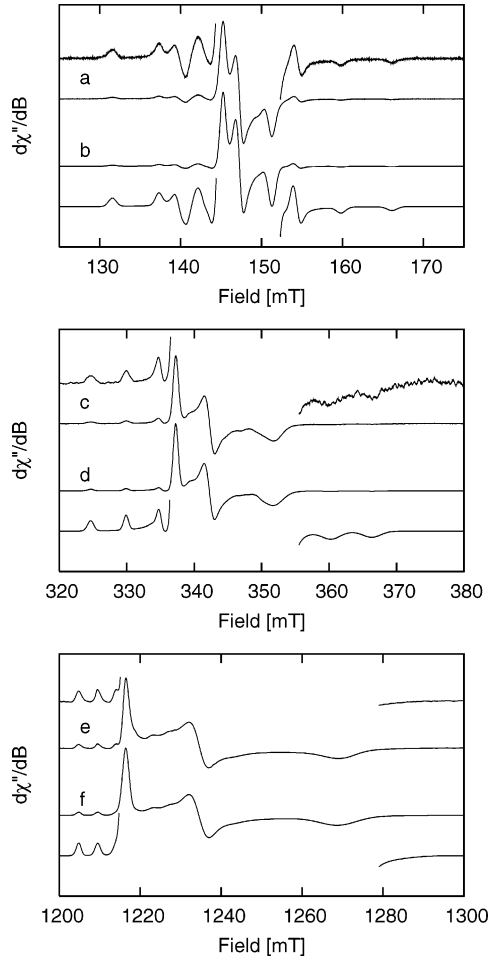

Figure 6. Multifrequency EPR spectra of Tp*MoS(tdt) at 130 K. (a) S-band experimental spectrum, $\nu = 4.0642$ GHz; (b) simulated S-band spectrum; (c) X-band experimental spectrum, $\nu = 9.4455$ GHz; (d) simulated X-band spectrum; (e) Q-band experimental spectrum, $\nu = 34.007$ GHz; and (f) simulated Q-band spectrum. (a,b) Insets expanded by 5.57 and 8.18, respectively; (c,d) low field insets expanded by 4.79 and 7.0, respectively, and high field insets expanded by 20.0 and 17.0, respectively; and (e,f) low field insets expanded by 2.73 and 4.0, respectively, and high field insets expanded by 2.73 and 8.0, respectively.

plexes, which possess only C_1 symmetry in the solid state, with the two phenolate groups coordinating in distinctly different orientations (Figures 2 and 4). These complexes exhibit relatively large $\langle A \rangle$ values in the vicinity of 45×10^{-4} cm^{-1}. The commonly observed inverse relationship between $\langle g \rangle$ and $\langle A \rangle$[20] is clearly followed, with the presence of at least one sulfur donor atom *cis* to the Mo≡S bond (bdt, tdt) resulting in a larger $\langle g \rangle$ being associated with a smaller value of $\langle A \rangle$, whereas oxygen donors give rise to smaller values of $\langle g \rangle$ associated with larger $\langle A \rangle$ parameters. The lower *g*-values of the monodentate complexes compared with the bidentate complexes suggests a lower SOMO−LUMO gap (eq 3), which is consistent with the lower d−d transition energy observed in the near-IR spectra (Table 1).

The magnitude and variation of the spin Hamiltonian parameters for the series of complexes in Table 5 reflect the orbital composition of the electronic ground and excited states, including the degree of metal−ligand covalency, configurational mixing (vide infra), and both metal and ligand spin-orbit coupling. The spin-orbit interaction, as a perturbation to the ligand field (LF), leads to small admixtures of excited states into the ground-state wavefunction. The electron Zeeman interaction therefore contains small contributions due to orbital angular momentum which shift the effective *g*-value from the free-electron value[48,62,63,64]

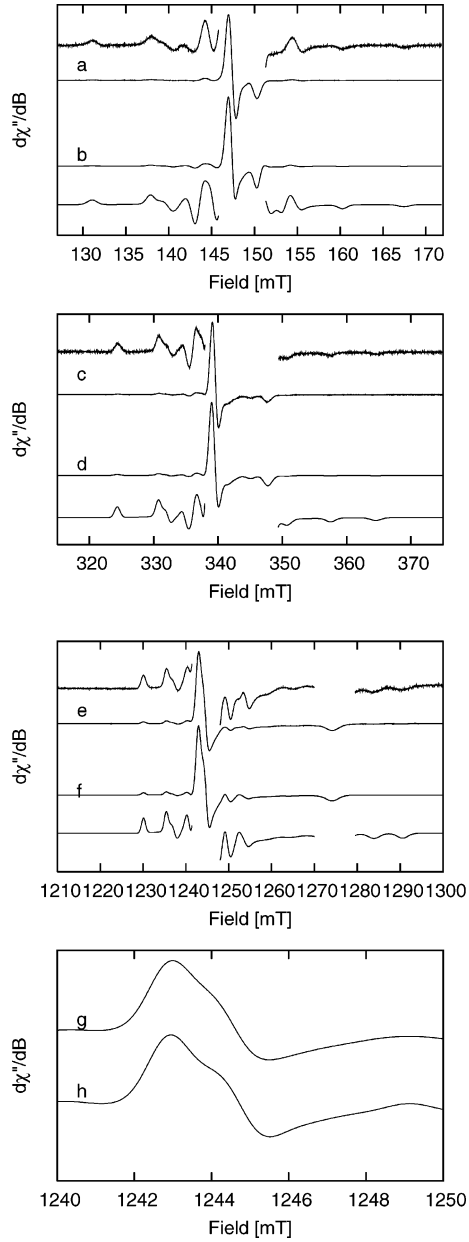

Figure 7. Multifrequency EPR spectra of Tp*MoO(cat) at 130 K. (a) S-band experimental spectrum, $\nu = 4.0478$ GHz; (b) simulated S-band spectrum; (c) X-band experimental spectrum, $\nu = 9.3412$ GHz; (d) simulated X-band spectrum; (e) Q-band experimental spectrum, $\nu = 34.230$ GHz; (f) simulated Q-band spectrum; (g,h) Expansion of the $g \sim 1.96$ region in the experimental and simulated spectra, respectively, showing the nonaxially symmetric **g** matrix; (a,b) Both insets expanded by a factor of 10.0; (c,d) Insets expanded by 12.0 and 10.0, respectively; (e) Low, mid, and high field insets expanded by 7.0, 7.0, and 15.0, respectively; and (f) Low, mid, and high field insets expanded by 7.0, 3.5, and 15.0, respectively.

(62) Pilbrow, J. R. *Transition Ion Electron Paramagnetic Resonance*; Clarendon Press: Oxford, 1990.
(63) Mabbs, F. E.; Collison, D. *Electron Paramagnetic Resonance of d Transition Metal Compounds*; Elsevier: Amsterdam, 1992.
(64) Chang, C. S. J.; Collison, D.; Mabbs, F. E.; Enemark, J. H. *Inorg. Chem.* **1990**, *29*, 2261.

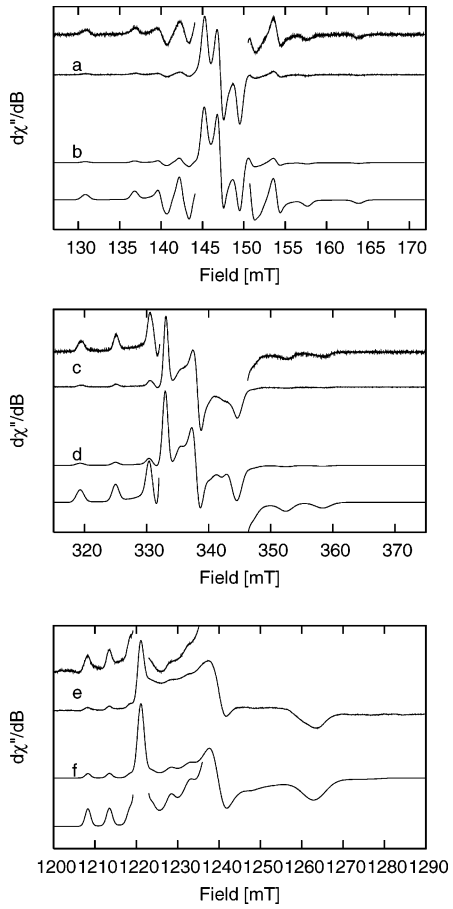

Figure 8. Multifrequency EPR spectra of Tp*MoO(bdt) at 130 K. (a) S-band experimental spectrum, $\nu = 4.0630$ GHz; (b) simulated S-band spectrum; (c) X-band experimental spectrum, $\nu = 9.3338$ GHz; (d) simulated X-band spectrum; (e) Q-band experimental spectrum, $\nu = 34.226$ GHz; and (f) simulated Q-band spectrum. (a,b) Both insets expanded by a factor of 5.0, respectively; (c,d) both insets expanded by a factor of 6.0, respectively; and (e,f) low field insets expanded by 5.0 and 3.0, respectively, and high field insets expanded by 4.0 and 3.0, respectively.

$$g_{ij} = g_e\delta_{ij} + \Delta g_{ij}^{\mathrm{d-d}} + \Delta g_{ij}^{\mathrm{MLCT}} + \Delta g_{ij}^{\mathrm{LMCT}}$$

$$= 2.0023\,\delta_{ij} - \sum_k \frac{F_k}{|\Delta E_k^{\mathrm{d-d}}|} - \sum_k \frac{G_k}{|\Delta E_k^{\mathrm{MLCT}}|} + \sum_k \frac{H_k}{|\Delta E_k^{\mathrm{LMCT}}|} \quad (3)$$

where the summation is over all transitions of appropriate type and ΔE_k is the excitation energy associated with each d−d, metal-to-ligand charge transfer (MLCT) and ligand-to-metal charge transfer (LMCT) transition. Here F_k, G_k, and H_k contain cross-terms between orbital Zeeman and spin−orbit coupling (SOC) matrix elements and depend on the composition of the ground, metal-centered, and ligand-centered excited states, in particular the degree of metal−ligand covalency and the magnitude of the ligand SOC. The magnitudes of the *g* shifts are also inversely proportional to the energy separation of the ground and excited states; thus in principle it is possible to correlate trends in the principal *g*-values with changes in the electronic absorption spectra, although excited states must also have appropriate symmetry to contribute to the *g* shifts. Intense charge transfer (CT) bands can also obscure the formally forbidden d−d transitions between metal-centered orbitals, as is presumably the case for Tp*MoS(cat), Tp*MoS(bdt), and Tp*MoS(tdt) (Table 1), which only exhibit intense CT bands. The d−d and MLCT transitions from the singly occupied molecular orbital to unoccupied MOs serve to lower the *g*-values, while LMCT transitions from doubly occupied MOs to the SOMO raise the *g*-values. If the LMCT states are close in energy to the ground state, or there are many such LMCT excitations, they may outweigh the negative contributions and produce *g* factors greater than g_e.

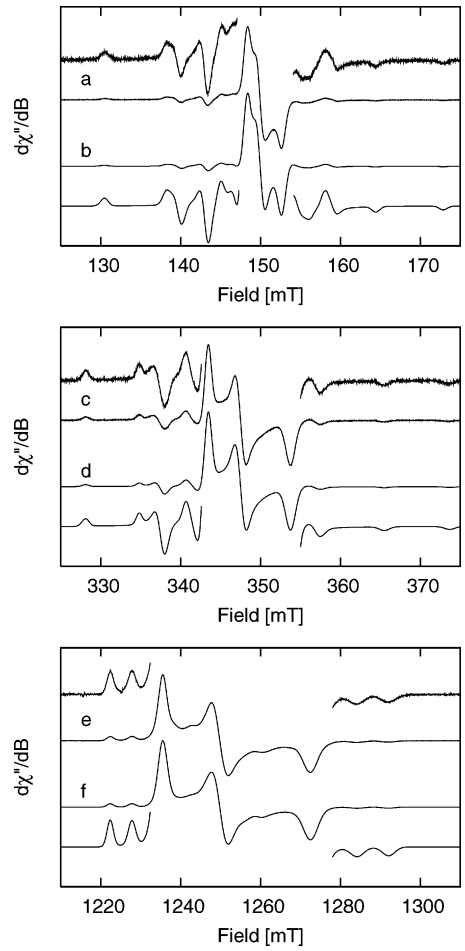

Figure 9. Multifrequency EPR spectra of Tp*MoO(etp)$_2$ at 130 K. (a) S-band experimental spectrum, $\nu = 4.0703$ GHz; (b) simulated S-band spectrum; (c) X-band experimental spectrum, $\nu = 9.4451$ GHz; (d) simulated X-band spectrum; (e) Q-band experimental spectrum, $\nu = 33.921$ GHz; and (f) simulated Q-band spectrum. (a,b) Insets expanded by 6.12 and 8.18, respectively; (c,d) insets expanded by 3.0 and 3.78, respectively; and (e,f) insets expanded by 5.56 and 8.0, respectively.

Crystal Field Description of Spin Hamiltonian Parameters. Large noncoincidence angles can be explained by a model in which extensive mixing among Mo 4d orbitals takes place. Although LMCT and MLCT states of appropriate symmetry may also contribute, for transition metals the dominant contribution to g_{ij} is usually $\Delta g_{ij}^{\mathrm{d-d}}$, which arises from transitions within the Mo 4d manifold. In C_s symmetry with a $\sigma^{(XZ)}$ mirror plane, in which the *X* axis lies between the metal−ligand bonds (Figure 1), the $d_{X^2-Y^2}$, d_{XZ}, and d_{Z^2} orbitals transform as A′ and the d_{XY} and d_{YZ} orbitals transform

as A″. The metal-based antibonding wavefunctions are therefore[41,63,65]

$$\psi^{a'*}_{X^2-Y^2} = \alpha[a_1 d_{X^2-Y^2} + b_1 d_{XZ} + c_1 d_{Z^2}]$$

$$\psi^{a'*}_{XZ} = \beta[a_2 d_{XZ} + b_2 d_{X^2-Y^2} + c_2 d_{Z^2}]$$

$$\psi^{a'*}_{Z^2} = \gamma[a_3 d_{Z^2} + b_3 d_{X^2-Y^2} + c_3 d_{XZ}]$$

$$\psi^{a''*}_{XY} = \delta[a_4 d_{XY} + b_4 d_{YZ}]$$

$$\psi^{a''*}_{YZ} = \epsilon[a_5 d_{YZ} + b_5 d_{XY}] \quad (4)$$

where, by definition, $a_q > b_q$, c_q ($q = 1,2,...$). Here covalency appears only implicitly through the metal-centered orbital coefficients $\alpha,...,\epsilon$. Since the molecular X and Y axes are placed between the metal−ligand bonds (Figure 1), the ground-state wavefunction is $\psi^{a'*}_{X^2-Y^2}$ (SOMO).

Making the reasonable assumption that the low symmetry is a perturbation to a tetragonal ligand field, we anticipate the lowest pair of excited states will be the π^* antibonding $\psi^{a'*}_{XZ}$ (LUMO+1) and $\psi^{a''*}_{YZ}$(LUMO) orbitals and the highest pair the σ-antibonding $\psi^{a''*}_{XY}$ and $\psi^{a'*}_{Z^2}$ orbitals, which are directed along the metal−ligand bonds.[48] The d−d transition energies in Table 1 are therefore related to energy differences between the $\psi^{a'*}_{XZ}$ and $\psi^{a''*}_{YZ}$ orbitals and the $\psi^{a'*}_{X^2-Y^2}$ orbital. The energy of these SOMO→LUMO,LUMO+1 transitions depends on the relative destabilization of these three antibonding orbitals, which will be related to the type of X_2 ligand(s) and their torsion angles. The π^* interactions of out-of-plane ligand p orbitals with the out-of-plane metal orbitals will destabilize $\psi^{a'*}_{XZ}$ and $\psi^{a''*}_{YZ}$, whereas the interaction of the SOMO with in-plane ligand orbitals (pseudo-σ^* interaction) will destabilize $\psi^{a'*}_{X^2-Y^2}$.[31] It is difficult to establish the energies of these molecular orbitals based on qualitative arguments alone; however, we note that the complexes with monodentate X ligands have very similar bond and torsion angles, which is consistent with their comparable SOMO−LUMO gaps.[66]

Electron Zeeman Matrix. Using the ground- and excited-state wavefunctions (4) in expression (3) and neglecting the CT contributions, the complete analytical form of the g shift is[41,63]

$$\Delta g^{d-d}_{ZZ} = -\frac{2\lambda_{Mo}\alpha^2\delta^2(2a_1a_4 + b_1b_4)^2}{\Delta E_{XY}} - \frac{2\lambda_{Mo}\alpha^2\epsilon^2(2a_1b_5 + b_1a_5)^2}{\Delta E_{YZ}}$$

$$\Delta g^{d-d}_{XX} = -\frac{2\lambda_{Mo}\alpha^2\delta^2[b_1a_4 + a_1b_4 + \sqrt{3}c_1b_4]^2}{\Delta E_{XY}} - \frac{2\lambda_{Mo}\alpha^2\epsilon^2[b_1b_5 + a_1a_5 + \sqrt{3}c_1a_5]^2}{\Delta E_{YZ}}$$

$$\Delta g^{d-d}_{YY} = -\frac{2\lambda_{Mo}\alpha^2\beta^2[(a_1a_2 - b_1b_2) + \sqrt{3}(b_1c_2 - c_1a_2)]^2}{\Delta E_{XZ}} - \frac{2\lambda_{Mo}\alpha^2\gamma^2[(a_1c_3 - b_1b_3) + \sqrt{3}(b_1a_3 - c_1c_3)]^2}{\Delta E_{3Z^2-R^2}}$$

$$\Delta g^{d-d}_{XZ} = \Delta g^{d-d}_{ZX} = \frac{2\lambda_{Mo}\alpha^2\delta^2(b_1a_4 + a_1b_4 + \sqrt{3}c_1b_4)(2a_1a_4 + b_1b_4)}{\Delta E_{XY}} + \frac{2\lambda_{Mo}\alpha^2\epsilon^2(b_1b_5 + a_1a_5 + \sqrt{3}c_1a_5)(2a_1b_5 + b_1a_5)}{\Delta E_{YZ}} \quad (5)$$

where λ_{Mo} is the molybdenum spin−orbit coupling constant and $\Delta E_i = |E(\psi_i) - E(\psi^{a'*}_{X^2-Y^2})|$ ($i = YZ, XZ, XY, Z^2$). Dominant contributions to both **g** anisotropy and noncoincidence with the molecular frame ($\Delta g_{XZ}{}^{LF} \neq 0$) will involve coupling of the major orbital component of low-lying excited states with the $d_{X^2-Y^2}$ character of the ground state, namely terms which multiply coefficients a_pa_q ($p \neq q = 1,2,...$). In this approximation, covalency effectively leads to an anisotropic reduction of the g shift via the dependence on the orbital coefficients $\alpha^2,...,\epsilon^2$.

Anisotropy of g_{xx} and g_{yy} in tetragonal symmetry results mainly from the energy difference between ΔE_{XZ} and ΔE_{YZ},[61] but configurational mixing in monoclinic symmetry enables additional SOC of the $\psi^{a'*}_{X^2-Y^2}$ ground state to excited states and leads to further contributions to the g shifts. In this respect, large admixtures should occur between states belonging to the same irreducible representation, provided they are sufficiently close in energy. Admixture of d_{XY} and d_{YZ} (b_4, $b_5 \neq 0$), for example, results in a rotation about the Y axis of the $\psi^{a''*}_{XY}$, $\psi^{a''*}_{YZ}$ pair as a unit and hence a rotation of the principal g_{xx} and g_{zz} directions, which will be approximately orthogonal to the planes of these orbitals, respectively.[14,65]

Influence of LMCTs. So far we have considered only the d−d contributions to the **g** matrix. The thiomolybdenyl model complexes all exhibit $g_{zz} < g_{yy} < g_{xx} < g_e$, where g_{zz} is significantly lower. However, the bis-dithiolene complexes have g_{xx} very close to g_e and for the molybdenyl analogue, Tp*MoO(bdt), it was found that $g_{xx} > g_e$.[67] This indicates there must be LMCTs involving sulfur-based donor orbitals which provide positive contributions to the **g** matrix (eq 3).

In a single-crystal study of Tp*MoOX$_2$ (X = F, Cl, Br), β was found to vary substantially across the series,[34]

(65) Scullane, M. I.; Taylor, R. D.; Minelli, M.; Spence, J. T.; Yamanouchi, K.; Enemark, J. H.; Chasteen, N. D. *Inorg. Chem.* **1979**, *18*, 3213.

(66) In making such comparisons, it must be borne in mind that there may be differences between the solid state and solution molecular structures.

(67) Note that this does not imply that SOC to LMCT donor orbitals provide g shifts arising purely from angular orbital momentum in the molecular X direction, because β is large and therefore $\hat{x}$ is expected to deviate substantially from $\hat{X}$. The orientation of the **g** and **A** matrices relative to the molecular axes and a discussion of the assignment of principal components will be discussed in detail ref 47.

suggesting that CT excited states are associated with the rotation of g_{zz} away from the molecular Z axis and confirming that the important CT transitions are controlled by the ligands *cis* to the terminal ligand.[41] However, halide ligands are free to rotate about the Mo−X bond axis, whereas steric constraints will place restrictions on the orientation of the O or S p orbitals of cat, bdt, and monodentate (OR) ligands relative to the Mo 4d orbitals. In the latter case, covalencyand the relative importance of CT transitions to the **g** matrix may be reduced. Support for this idea comes from the fact that the atomic SOC constant for O(2p) (150 cm^{-1}) is less than half that of S(3p) (370 cm^{-1}),[63] and yet β is significant for catecholate and phenolate complexes also. Nonetheless, the g-values of Tp*MoS(bdt) and Tp*MoS(tdt) are increased compared with Tp*MoS(cat), in particular g_{xx}, while β is decreased. This suggests that LMCTs involving S-based donor orbitals are still important but that they modulate the large rotation angle whose source primarily derives from d−d transitions.

Nuclear Hyperfine Matrix. Neglecting terms in $1/\Delta E_i$, the components of the hyperfine matrix in $C_s^{(XZ)}$ symmetry are[41,63]

$$A_{ZZ} \approx P\left[-\alpha^2\kappa - 2\frac{\alpha^2}{7}(4a_1^2 + b_1^2 - 2) + \Delta g_{ZZ}\right]$$

$$A_{XX} \approx P\left[-\alpha^2\kappa - 2\frac{\alpha^2}{7}(a_1^2 + b_1^2 + 3c_1^2 + 2\sqrt{3}\,a_1c_1 - 2) + \Delta g_{XX}\right]$$

$$A_{YY} \approx P\left[-\alpha^2\kappa - 2\frac{\alpha^2}{7}(a_1^2 + 4b_1^2 + 3c_1^2 + 2\sqrt{3}\,a_1c_1 - 2) + \Delta g_{YY}\right]$$

$$A_{XZ} = A_{ZX} \approx P\left[2\frac{\alpha^2}{7}(3a_1b_1 + \sqrt{3}\,b_1c_1 - 2) + \Delta g_{XZ}\right] \qquad (6)$$

where $P = g_e\beta_e g_n\beta_n \langle r^{-3}\rangle_{4d}$, κ represents the Fermi contact interaction due to unpaired electron spin density at the nucleus (core polarization), and the remaining terms result from spin-orbit contributions. Configurational mixing in the ground state (b_1,$c_1 \neq 0$) is seen to influence the anisotropic hyperfine interaction. The magnitude of the isotropic contact interaction κ, on the other hand, is determined by the unpaired spin density at the nucleus and the degree of covalency of the ground-state $\psi^{a'*}_{X^2-Y^2}$. Increasing covalency leads to an increase in g_{ij} values (eq 5) and a concomitant reduction in A_{ij} values (eq 6). This yields the familiar inverse relationship between $\langle g\rangle$ and $\langle A\rangle$ commonly observed in many instances.[51,64] Figure 10 displays this behavior, with the electron withdrawing ene-1,2-dithiolate ligands possessing the highest $\langle g\rangle$ and the lowest $\langle A\rangle$. Some clustering of data can also be seen for complexes containing similar donor ligands and terminal groups. It is interesting to note, however, that the trend of decreasing hyperfine coupling in the order Mo≡O > Mo≡S observed for $MoE(NRAr)_3$ complexes[46] does not hold for the present Tp^*MoEX_2 series. This may be due to

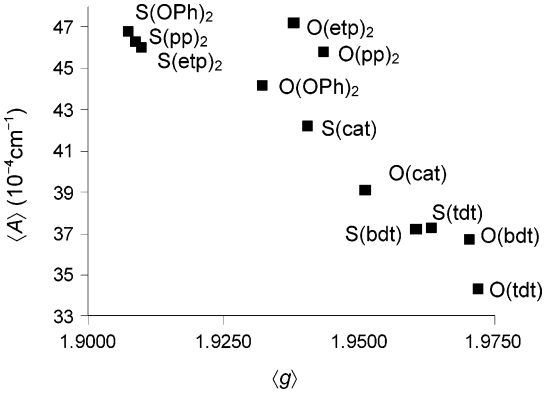

Figure 10. Inverse correlation of $\langle g\rangle$ and $\langle A\rangle$ (^{95}Mo) for the complexes listed in Table 5. Points are labeled with the EX_2 portion from the corresponding formula Tp^*MoEX_2.

differences in core polarization κ rather than covalency; however, there is no simple way to predict the variation of this quantity at this simple level of theory.

The orientation of **A**(^{95,97}Mo) is primarily determined by the first-order dipolar interaction (terms in parentheses in eq 6), which depends on the ground-state orbital coefficients a_1, b_1, and c_1 and hence the shape and orientation of the SOMO. In particular, an admixture of d_{XZ} into the ground state ($b_1 \neq 0$) will result in a rotation about the Y axis of $\psi^{a'*}_{X^2-Y^2}$ out of the X,Y plane. Since the largest principal component, $A_{z'z'}$, will be roughly perpendicular to the plane of the SOMO, it will therefore be rotated away from the molecular Z axis. On the other hand, admixture of d_{Z^2} character ($c_1 \neq 0$) into the SOMO results in a "rhombic distortion"[68,69] by augmenting ($c_1 < 0$) or diminishing ($c_1 > 0$) the positive lobes of $\psi^{a'*}_{X^2-Y^2}$ and vice versa for the negative lobes. Appreciable admixture is only expected when orbitals are energetically close and hence the magnitudes of b_1 and c_1 will be small; a rhombic distortion is less likely since $\psi^{a'*}_{Z^2}$ will be relatively much higher in energy compared with $\psi^{a'*}_{XZ}$.[48] Since we anticipate that the $A_{x'x'}$ and $A_{y'y'}$ principal components will be directed approximately along the lobes of the magnetic orbital, a negligible "rhombic distortion" ($c_1 \approx 0$) appears consistent with the observation that $A_{x'x'} \approx A_{y'y'}$ in our simulations (Table 5). These arguments naturally extend to C_1 symmetry, with possible admixtures of d_{YZ} and d_{XY} permitting further rotation of the SOMO, and hence **A**, about the X and Z axes, respectively.

Noncoincidence Angles. It is usually expected that the rotation of **A**(^{95,97}Mo) is small and that its principal directions therefore lie reasonably close to the molecular axes defined in Figure 1, $A_{z'z'}$ being associated with the Mo≡E bond direction. Thus the noncoincidence of the principal axes of the **g** and **A** interactions arises from the difference between the relatively large rotation of **g** from the molecular axes and the relatively small rotation of **A**. Randomly oriented EPR spectra are only capable of yielding this relative difference. Such "powder patterns" can be difficult to

(68) Hitchman, M. A.; Olson, C. D.; Belford, R. L. *J. Chem. Phys.* **1969**, *50*, 1195.
(69) Belford, R. L.; Harrowfield, B.; Pilbrow, J. R. *J. Magn. Reson.* **1977**, *28*, 433.

simulate when low natural isotopic abundances ($I = 5/2$, ~ 25%) and strain broadening limit sensitivity and resolution. Multifrequency EPR has aided the extraction of suitable low-symmetry spin Hamiltonian parameters by enhancing *g* value resolution at Q-band due to larger Zeeman splitting (e.g. Figures 5 and 7) and by improving hyperfine resolution at S-band due to reduced *g*-*A* strain and enhanced state-mixing effects on resonant field positions.

In contrast with the present results, the parameters obtained previously for Tp*MoO(bdt)[48] and Tp*MoO(cat)[49] suggested orthorhombic **g** and **A**, which required very different relative magnitudes of the principal hyperfine components. In particular, for Tp*MoO(bdt) (and also the related Tp*MoO(edt)[48]), $A_{y'y'}$ was very small (3.3×10^{-4} cm^{-1} for the latter complex) and $A_{x'x'} \sim A_{z'z'}$. However, referring to eq 2, it is evident that an equal first-order splitting of $A^2 = [A_{x'x'}^2 + A_{z'z'}^2]/2$ along both the principal g_{xx} and g_{zz} directions can also be obtained for any values of $A_{x'x'}$ and $A_{z'z'}$ in monoclinic symmetry when $\beta \sim 45°$. Using the X-band simulation parameters of Dhawan and Enemark[48] for Tp*MoO(bdt) (Table 5) appears to produce a satisfactory simulation at X-band (Figure S1(b),(c), Supporting Information). Compared with our monoclinic parameters, there should exist appreciable difference toward the center of the $I = 5/2$ hyperfine powder pattern, although the more intense anisotropic $I = 0$ (75%) resonances and residual line widths mask these differences so that either set appears reasonable. At S-band (Figure S1(a),(b)), however, marked differences become apparent. The use of orthorhombic parameters fails to simultaneously reproduce the experimental spectra of this series of complexes at S-band frequencies, and only a genuine low-symmetry spin Hamiltonian is found to be satisfactory at all microwave frequencies. This highlights the immense value of performing multifrequency EPR experiments. While at S- and X-band microwave frequencies, the **g** matrix for Tp*MoO(cat) appears to be axially symmetric (Figure 7a−d and ref 49), the greater *g*-value resolution at Q-band frequencies (Figure 7e−h) reveals a **g** matrix of at most orthorhombic symmetry for Tp*MoO(cat). Computer simulation of the multifrequency spectra with a single set of parameters (Table 5) also shows that this Mo center also has C_s monoclinic symmetry. These results are consistent with a subsequent theoretical study of the thiomolybdenyl complexes and related molybdenyl analogues,[47] where it is shown that the spin Hamiltonian for both Tp*MoO(cat) and Tp*MoO(bdt) is indeed predicted to be low symmetry and that large noncoincidence angles arise, consistent with the other complexes in the series.

Relevance to Mo Enzymes. A comparison of the **g** and **A** matrices for the very rapid Mo(V) species in xanthine oxidase with those for the oxo and sulfido Mo(V) complexes (Table 5) reveals that the magnitude of the *g* and *A* values for the very rapid Mo(V) species are more consistent with those complexes which have a terminal oxo ligand. This is in agreement with the most recent diffraction data on the enzyme[12] and the EPR data (**A**(^{95}Mo, ^{98}Mo, ^{33}S, and ^{17}O)) from a series of oxosulfido complexes. Interestingly, the rhombicity (Table 5) of the very rapid Mo(V) species is significantly larger than the model complexes, with the largest *g*-value (g_{xx}) being significantly greater than the free electron *g*-value. This may be attributed to either configurational mixing and/or LMCTs (vide supra) involving sulfur based donor orbitals.

The metal-di(thi)olate fold angle has recently been implicated as a key factor in the ability of the pterin ring to fine-tune the electron density at the active site of xanthine oxidase enzymes. DFT studies of model complexes derived from the crystal structure of aldehyde oxidase indicate the acceptor LUMO in the oxidized active site possesses a fold angle >30° larger than the SOMO of the reduced active site.[70] Furthermore, a relevant DFT study has recently been performed on the geometry-optimized structure of Tp*MoO(bdt) to determine its frontier orbitals.[71] The optimization increased the fold angle from 21° in the solid state to 31° in the gas phase. This raises the question as to whether variations in a fold angle can be probed via changes in spin Hamiltonian parameters. In Table 6 we list the Mo-di(thi)olate fold angles for the bidentate complexes and contrast them with the experimental **g** and **A** noncoincidence angles. Given the variation in β between the O- and S-donor thiomolybdenyl complexes presented herein, it is not surprising that no clear relationship between the fold angle and the β rotation can be established. This point will, however, be revisited in a companion study.[47]

Conclusions

We have generated an extended series of mononuclear, thiomolybdenyl complexes, Tp*Mo^{V}SX$_2$, containing a variety of coligands X/X$_2$. These have been characterized by microanalysis, mass spectrometry, IR, EPR, UV−visible spectroscopy, and a number of crystal structures have been determined. The molybdenyl analogues Tp*MoO(etp)$_2$, Tp*MoO(pp)$_2$, Tp*MoO(cat), and Tp*MoO(bdt) were also generated and studied. Multifrequency EPR spectroscopy has proven invaluable in extracting low-symmetry spin Hamiltonian parameters which might otherwise be unobtainable from X-band spectra alone. The trends from our data have enabled us to propose a revised interpretation of the electronic structure for Tp*MoO(cat) and Tp*MoO(bdt).

Understanding the electronic origin of **g** and **A**(^{95,97}Mo) noncoincidence is important, as it relates directly to the degree of d orbital and charge-transfer excited-state mixing in low-symmetry molybdenyl sites, and the results obtained herein have implications for the understanding of oxosulfido-Mo(V) centers implicated in the turnover of the enzymes, such as the very rapid EPR signal in xanthine oxidase. In a simplified crystal field model, the sizable Euler angle β can only originate from a difference between a rotation of **g** (via admixture of the d_{XY} and d_{YZ} orbitals) and a rotation of **A** (via an admixture of d_{XZ} and $d_{X^2-Y^2}$ orbitals). However, the admixture of d_{XY} and d_{YZ} is not expected to be large. In a

(70) Joshi, H. K.; Enemark, J. H. *J. Am. Chem. Soc.* **2004**, *126*, 11784.

(71) Joshi, H. K.; Cooney, J. A.; Inscore, F. E.; Gruhn, N. E.; Lichtenberger, D. L.; Enemark, J. H. *Proc. Natl. Acad. Sci.* **2003**, *100*, 3719.

Table 5. Anisotropic Spin Hamiltonian Parameters for Mo(V) Model Complexes Determined from the Computer Simulation of Both Room Temperature and Frozen Solution (130 K) Multifrequency EPR Spectra[i]

complex	g_{xx}	g_{yy}	g_{zz}	$\langle g\rangle^g$	anisotropy[a]	rhombicity[b]	$A_{x'x'}$	$A_{y'y'}$	$A_{z'z'}$	$\langle A\rangle^g$	α^h	β	γ
Tp*MoS(etp)$_2$	1.9558	1.9114	1.8623	1.9098	0.0935	0.4749	32.0	34.0	72.0	46.0	0	26	0
Tp*MoO(etp)$_2$	1.9647	1.9417	1.9073	1.9379	0.0574	0.4007	33.0	34.0	74.5	47.2	0	26.5	0
Tp*MoS(pp)$_2$	1.9575	1.9111	1.8575	1.9087	0.1000	0.4640	33.0	34.0	72.0	46.3	0	25	0
Tp*MoO(pp)$_2$	1.9683	1.9456	1.9162	1.9434	0.0521	0.4357	32.0	34.0	71.5	45.8	0	36	0
Tp*MoS(OPh)$_2$	1.9550	1.9110	1.8562	1.9074	0.0988	0.4453	33.5	34.5	72.5	46.8	0	24	0
Tp*MoO(OPh)$_2$[c]	1.959	1.938	1.901	1.932	0.058	0.362				44.2			
Tp*MoS(cat)	1.9646	1.9595	1.8970	1.9404	0.0676	0.0754	30.0	29.0	67.5	42.2	0	34.5	0
Tp*MoO(cat)	1.9680	1.9660	1.9194	1.9511	0.0486	0.0412	27.0	26.0	64.2	39.1	0	36	0
Tp*MoO(cat)[d]	1.969	1.969	1.920	1.953	0.049	0.000	34.0	20.0	66.2	40.1	0	0	0
Tp*MoS(bdt)	1.9975	1.9680	1.9159	1.9605	0.0816	0.3615	26.0	26.5	59.2	37.2	0	39	0
Tp*MoO(bdt)	2.0025	1.9730	1.9360	1.9705	0.0665	0.4436	24.0	26.0	60.0	36.7	0	45	0
Tp*MoO(bdt)[e]	2.004	1.972	1.934	1.970	0.070	0.457	50.0	11.4	49.7	37.0	0	0	0
Tp*MoS(tdt)	2.0007	1.9714	1.9177	1.9633	0.0830	0.3530	26.0	27.0	58.8	37.3	0	38.5	0
Tp*MoO(tdt)[c]	2.004	1.974	1.937	1.972	0.067	0.448				34.3			
very rapid, XO[f]	2.0252	1.9550	1.9494	1.9765	0.0758	0.9261	19.1	18.2	44.4	27.2	−5.8	54.4	9.9

[a] Anisotropy $= g_{xx} - g_{zz}$. [b] Rhombicity $= |(g_{xx} - g_{yy})/(g_{xx} - g_{zz})|$. [c] Reference 51. No anisotropic hyperfine data available. [d] Reference 49. [e] Reference 48. [f] Reference 7 (Wilson et al.). [g] $\langle g\rangle = 1/3(g_{xx} + g_{yy} + g_{zz})$, $\langle A\rangle = 1/3(A_{x'x'} + A_{y'y'} + A_{z'z'})$. Units for coupling constants $= 10^{-4}$ cm^{-1}. [h] Euler rotations are defined as $R = R_z(\gamma)R_y(\beta)R_z(\alpha)$. [i] Previous (high symmetry) data by other workers are provided for Tp*MoO(bdt) and Tp*MoO(cat) for comparison.

Table 6. Important Bond and Torsion Angles in Tp*MoEX$_2$ Complexes, as Obtained from Available X-ray Crystallographic Structures[c]

complex	E≡Mo−X	E≡Mo−Y	Mo−X−C	Mo−Y−C	E≡Mo−X−C	E≡Mo−Y−C	Mo-di(thi)olate fold angle	β (°)
Tp*MoO(cat)[a]	102	101	112	113	−83	82	18.3	36
Tp*MoS(cat)	101	102	112	113	−79	78	21.1	34.5
Tp*MoO(bdt)[b]	101	101	104	104	−81	82	21.3	45
Tp*MoS(bdt)	101	101	104	104	−78	78	25.3	39
Tp*MoO(etp)$_2$	101	105	134	139	−42	−105		26.5
Tp*MoS(etp)$_2$	101	104	134	141	−49	−108		26
Tp*MoS(pp)$_2$	104	101	144	135	115	55		25

[a] Structure taken from Tp*MoO(catCl$_4$), ref 49. Euler angle derived from this EPR study. [b] Structure taken from ref 48. Euler angle derived from this EPR study. [c] Relative to Figure 1, X(Y) refers to the directly coordinated atom of the X_2 donor ligand (X_2 = cat, bdt, etp$_2$, pp$_2$) that projects out of (into) the page. No structural information is available for Tp*MoE(OPh)$_2$ (E = O,S) or Tp*MoO(pp)$_2$.

ligand field model, charge-transfer transitions can also contribute; however, a large noncoincidence angle is not expected to arise solely due to ligand orbital angular momentum of the donor orbitals, because the Euler rotation is observed to be large for both the thiomolybdenyl catecholate and benzene-dithiolate complexes, yet the atomic SOC constants of O(2p) and S(3p) differ by more than a factor of 2. More subtle contributions from the equatorial donor ligands are predicted to arise from LMCT transitions, which lead to one of the principal g-values being near the free electron value for the bdt and tdt complexes. This, in addition to the inherent ambiguities associated with spectral fitting of low-symmetry EPR spectra, underscores the need for detailed studies of the electronic structure.

An LCAO-MO model incorporating LMCT effects has recently been used to evaluate both Δg_{ij}^{LF} and Δg_{ij}^{LMCT} contributions to the EPR spectra of molybdenyl halide complexes in C_{4v} symmetry[21] incorporating the directly coordinated nearest-neighbor atoms. Unfortunately, the number of free parameters is quite large, so that generalization of this approach to obtain the analytical form of Δg_{ij} in C_s symmetry becomes unwieldy due to the added complication of configurational mixing of orbitals. A number of assumptions about certain highly correlated parameters must also be made[63] which makes this approach unattractive. Computational methods, on the other hand, have rapidly matured to the point where they are capable of reasonably predicting the electronic structure and EPR spectral parameters of Mo model complexes. Neese and co-workers[39] have recently demonstrated this in a density functional study of the *cis,trans*-(L-N$_2$S$_2$)Mo^{V}OX [L-N$_2$S$_2$H$_2$ = *N,N*′-bis(mercaptophenyl)-1,2-diaminoethane] series of complexes. Using a similar approach, we have carried out a theoretical study of the electronic structure of a selected number mononuclear Tp*MoEX$_2$ (E = O,S) complexes, the results of which appear in a subsequent article.[47] This overcomes many of the approximations usually made in interpreting EPR spectra and enables a clearer connection between the electronic structure and the randomly oriented EPR spectra.

Acknowledgment. We gratefully acknowledge the financial support from the Australian Research Council, and we would also like to thank the EPR Division of Bruker Biospin for the Q-band measurements of the molybdenyl complexes Tp*MoO(cat) and Tp*MoO(bdt).

Supporting Information Available: X-ray crystallographic files for Tp*MoS(cat), Tp*MoS(pp)$_2$, and Tp*MoO(etp)$_2$ in CIF format, isotropic spin Hamiltonian parameters for Mo(V) model complexes determined from room-temperature S- and X-band EPR spectra (Table S1), and a comparison of simulated EPR spectra for Tp*MoO(bdt) (Figure S1) and Tp*MoO(cat) (Figure S2) in orthorhombic and monoclinic (C_s) symmetries. This material is available free of charge via the Internet at http://pubs.acs.org.

IC060585J